Binary alloy solidification and freckle formation: Effect of shrinkage induced flow on solutal instability and macro-segregation

Cite as: Phys. Fluids **33**, 037108 (2021); https://doi.org/10.1063/5.0039003
Submitted: 29 November 2020 . Accepted: 02 February 2021 . Published Online: 09 March 2021

Aniket D. Monde, Amit Shrivastava, Amman Jakhar, and Prodyut R. Chakraborty

Physics of Fluids ARTICLE scitation.org/journal/phf

Binary alloy solidification and freckle formation: Effect of shrinkage induced flow on solutal instability and macro-segregation

Cite as: Phys. Fluids **33**, 037108 (2021); doi: 10.1063/5.0039003
Submitted: 29 November 2020 · Accepted: 2 February 2021 ·
Published Online: 9 March 2021

Aniket D. Monde,[1] Amit Shrivastava,[1] Amman Jakhar,[2] and Prodyut R. Chakraborty[1,a)]

AFFILIATIONS

[1]Department of Mechanical Engineering, Indian Institute of Technology Jodhpur, Jodhpur 342037, India
[2]School of Mechanical Sciences, Indian Institute of Technology Bhubaneswar, Bhubaneswar 752050, India

[a)]Author to whom correspondence should be addressed: pchakraborty@iitj.ac.in

ABSTRACT

Freckle formation during directional solidification of binary alloy is a well-researched subject area. However, the influence of shrinkage induced flow (SIF) on freckling phenomena is barely reported. The focus of this work is to investigate this effect during bottom-up solidification of binary alloys. A fixed grid-based numerical scheme involving volume averaging of conserved parameters is proposed. The solidification geometry under consideration is a two-dimensional mold cavity with a central riser allowing continuous melt flow into the cavity. Model validation is obtained against existing numerical results involving directional solidification of Al-4.1 wt. % Cu alloy. However, heavier solute (Cu) rejection in the melt during solidification renders the validation case study devoid of freckling phenomena. The postvalidation investigations involve bottom up solidification of Al-30 wt. % Mg alloy with lighter solute (Mg) rejection, leading to solutal instability and freckle formation. The effect of SIF on solutal instability, channel formation, and overall macro-segregation is investigated. The intensity of SIF hinges on both cooling condition and opening size. The penetration depth of SIF into the solidification domain gives rise to either early or late onset of solutal instability. SIF penetration depth till the melt domain adjacent to the mushy layer promotes early onset of solutal instability. However, SIF penetration into the mushy layer itself triggers redistribution of solute-rich melt inside this layer, leading to delayed onset of solutal instability. Since the macro-segregation is a direct consequence of advection of solute inside and adjacent to the mushy region, the influence of SIF is manifested by unprecedented macro-segregation pattern.

NOMENCLATURE

Variables

C	species concentration
c_p	specific heat (J/kgK)
D_l	liquid solute diffusivity (m^2/s)
f	mass fraction
g	volume fraction
g_a	gravitational acceleration (m/s^2)
h	enthalpy (J/kg)
H	height (mm)
h_c	heat transfer coefficient (W/m^2K)
h_{sl}	latent heat (J/kg)
k	thermal conductivity (W/mK)
k_p	partition coefficient
p	pressure (Pa)
T	temperature (K)
T_c	cold boundary temperature (K)
T_m	melting temperature (K)
T_{liq}	liquidus temperature (K)
u, v	magnitude of velocity in x and y direction, respectively (mm/s)
V	velocity vector (m/s)
W	width (mm)
x, y	coordinate axes

Greek symbols

β_C	solutal expansion coefficient
β_T	thermal expansion coefficient (K^{-1})
ε	constant

λ relaxation factor
μ viscosity (kg/ms)
ρ density (kg/m^3)

Subscripts

C cavity
e eutectic
i, 0 initial
l liquid
s solid
ref reference value

I. INTRODUCTION

During the solidification process of both metallic and nonmetallic alloys, the melt undergoing the process manifests three distinct regions containing three different phases. These three distinct regions consist of pure solid, pure liquid, and mushy phase characterized by the coexistence of both solid and liquid phases. Unidirectional solidification in the bottom-up direction promotes two entirely different variations of mushy zone formation depending upon the solute-solvent constituent of the alloy system. Since the solubility of the solid phase is always less than that of the liquid phase, liquid to solid phase transformation causes solute rejection in the melt adjacent to the newly transformed solid region. As a result, the melt adjacent to the solid regions gets enriched in solute content, and a strong solute concentration is established in the melt adjacent to the solid phase. If the solute is heavier than the solvent, then the solute-rich melt adjacent to the solid phase gets heavier. In the case of bottom-up solidification orientation, the melt is stably stratified when it comes to the thermal buoyancy effect. The heavier solute rejection to the melt due to solid formation at the bottom during bottom-up solidification reinforces this stability of the buoyancy field, leading to a rich solute concentration near the bottom surface, known as inverse segregation. For alloy systems with heavier solute and lighter solvent, the mushy region manifests a planer front growth with inverse segregation. On the other hand, if the solute is lighter than the solvent, then the rejected excess solute in the melt adjacent to the solid region causes instability in the solutal buoyancy field. If this instability in the solutal buoyancy field is strong enough to overcome the stability of the thermal buoyancy field, the convection in the form of plume ensues. As a result, the mushy region is typically characterized by interspersed channels formations at the plume locations. Therefore, melt flow during solidification of alloys defined by the solutal buoyancy field has a profound effect on the growth of the mushy region and hence the overall macro-segregation. The presence of shrinkage induced flow and its interaction with the solutal convection augments the challenges associated with modeling of mushy front growth and overall macro-segregation further. In essence, a realistic prediction of overall macro-segregation for the bottom-up alloy solidification process must account for the interaction between shrinkage induced and solutal convection within the solidification domain.[1,2] Since the bottom-up solidification process is of primary interest to many industrial applications involving single crystal growth, understanding the combined effect of shrinkage induced and solutal convection on overall macro-segregation is of utmost importance.

In a bottom cooled cavity, the growth of a solid front occurs along a vertically upward direction. The thermal gradient along the vertically upward direction is positive with a stably stratified thermal buoyancy field. The thermal expansion coefficient is positive without any ambiguity, indicating the expansion of overall volume with increasing temperature and vice versa. However, depending on the relative heaviness or lightness of the solute with respect to the solvent, the solutal expansion coefficient needs to be assigned with negative or positive values. If the rejected solute to the melt during the alloy solidification process is heavier than the solvent, the solutal expansion coefficient is negative, indicating overall volume reduction of solute enriched melt. For bottom-up solidification orientation, the negative solutal expansion coefficient leads to stable stratification of the solutal buoyancy field, reinforcing a stably stratified thermal buoyancy field. On the other hand, the rejection of lighter solute in the melt during the alloy solidification process assigns a positive solutal expansion coefficient, indicating an overall volume expansion of the solute enriched melt. For directional alloy solidification with bottom cooling orientation, volume expansion of solute enriched melt adjacent to the growing solid front from the bottom promotes instability of the solutal buoyancy field that might lead to the formation of plumes.

The formation of the mushy region extending between the pure solid and pure liquid region can also be explained by the solute rejection phenomena during liquid to solid phase transformation process.[1,3–10] Since the melt adjacent to the newly transformed solid-phase gets enriched with solute concentration, a depression of liquidus temperature occurs for the solute-rich melt. This depression of liquidus temperature causes a delay in the further solidification process of the liquid-rich melt. Meanwhile, the regions beyond the solute-rich melt with leaner solute concentration and higher liquidus temperature cools down sufficiently to attain this comparatively higher liquidus temperature. As a result, liquid to solid phase transition ensues beyond the region with solute-rich melt causing farther solute rejection and farther spreading of a region with solid-phase dispersed within a solute-rich melt. However, the region adjacent to the cold boundary being the coldest region, complete solidification is eventually attained in this region with the local temperature approaching the eutectic temperature of the alloy system. Thus, we obtain a solidification domain characterized by a pure solid and liquid region separated by a region of dispersed solid phase within a solute-rich melt known as mushy region. Since the solutal gradient in the melt is predominant within the mushy region, the instability of the solutal buoyancy field primarily ensues from the mushy region itself. Depending on the strength of this instability, the effect can be farther propagated to the pure liquid region. The aiding or opposing nature of the interaction between the thermal and solutal buoyancy fields regulates the melt convection within and beyond the mushy region, defining its growth.[11–13] Since macro-segregation in the final cast product is of direct consequence of the mushy zone growth mechanism, it is extremely important to study the effect of solutal instability on the evolution of the mushy region.

Inverse segregation encountered due to the heavier solute rejection in the melt during solidification of the binary alloy has been studied and explained by several researchers.[14–17] Similarly, channel formation in the mushy region due to lighter solute rejection in the melt during the directional solidification of metal alloys[11,12,18] or inorganic alloys[19–23] is a well-studied subject area for many decades. Simulations considering shrinkage induced flow performed by Diao and Tsai,[14] and Chen and Tsai[15] successfully predicted the inverse segregation during the bottom-up solidification of Al–Cu alloy. However,

the model binary system considered,[14,15] is not conducive to promote freckle formation due to heavier solute rejection in the melt during the liquid–solid phase transition. Chiareli *et al.*;[24] Chiareli and Worster[25] considered the effect of a density difference between fluid and solid, in the absence of solutal buoyancy effect and analyzed the mushy layer instability with the conclusion that the instability can occur only in the case of expansion. Numerical models proposed by Schulze and Worster,[26] and Chung and Worster[27] were distinctly focused on obtaining steady-state solutions for the problems with specified channel positions. However, these models do not address the cause and onset of channel formation; neither do they analyzed the flow interaction between the adjacent channels. Katz and Worster[28] proposed a 2D numerical model based on Darcy's law and the enthalpy method, to avert imposing explicit conditions on the solid–mushy–liquid interfaces. The analysis was performed using NH_4Cl-H_2O solution, and the results obtained were compared with the experimental data presented by Peppin *et al.*[29] Further, Chakraborty and Dutta[30] numerically modeled the freckle formation during bottom-up solidification of NH_4Cl-H_2O solution. The detachment and advection of solid particles along with the melt were observed experimentally and implemented numerically. However, the shrinkage effect was unaccounted for during the solidification process. Recently, an experimental investigation was carried out by Kumar *et al.*[31] to address the effect of solutal composition over freckle formation for NH_4Cl-H_2O binary solution. The study was further extended to investigate the role of mushy zone permeability in driving the buoyancy flow patterns in faceted and dendritic growth during bottom-up solidification of KNO_3-H_2O and NH_4Cl-H_2O binary solution, respectively.[32] The results showed a peculiar behavior of decreasing and sudden increase in temperature during solidification for KNO_3 aqueous solution as compared to monotonous decrease in temperature for NH_4Cl-H_2O solution. In addition to double-diffusive convection during directional solidification, Anderson and Worster,[33] Guba and Worster,[34] and Roy *et al.*[35] studied an oscillatory instability within the mushy region, which was later modified for ternary alloy system by Guba and Anderson.[36]

Although the effect of shrinkage induced flow has been considered for the micro-scale solidification[37–39] and at macro-scale to model inverse segregation associated with heavier solute rejection during bottom-up solidification of aluminum-4.1 wt. % Copper alloy,[14,15] studies involving the effect of shrinkage induced flow on freckle formation is rarely found.[40] Challenges associated with the modeling of freckling phenomena during directional solidification of the binary alloy due to rejection of lighter solute in the melt become much more formidable when additional complexities involving the inclusion of shrinkage induced flow is accounted. Therefore, modeling channel formation in the mushy region and associated macro-segregation arising from the coupled interaction between shrinkage induced and solutal convection poses a very interesting endeavor. Since no such study has been reported so far, this work focuses on developing a numerical model to study the effect of shrinkage induced flow on freckle formation during bottom-up directional solidification of metal alloys. The solid–mushy and mushy–liquid interface is captured by employing the novel volume fraction updating method based on the fixed grid method. Before conducting the study involving the effect of shrinkage induced flow on channel formation, the model is validated with the existing results concerning inverse segregation investigation associated with heavier solute rejection in the melt during bottom-up solidification of aluminum-4.1 wt. % copper binary alloy.[14,15] Once the validation of the present model provided reasonable agreement with the existing results, we extended our study to analyze the interactions between the shrinkage induced flow and solutal instability associated with freckle formation during bottom-up solidification of model binary alloy system aluminum-30 wt. % magnesium. The study is aimed at obtaining a realistic prediction of freckle formation and corresponding macro-segregation during directional solidification of binary alloys under the influence of shrinkage induced flow.

II. MATHEMATICAL FORMULATION

The present numerical model is based on the continuum formulation originally developed by Bennon and Incropera,[41,42] and later suitably modified by Chiang and Tsai[43] to include the shrinkage induced flow effect. Governing equations are derived on the basis of the following assumptions: (a) the individual phases are homogeneous and isotropic, (b) the properties within an individual phase are constant but different in different phases, (c) phases satisfy thermodynamic equilibrium within the binary zone, and (d) relative velocity of solid phase is zero. Following these assumptions, the governing equations for continuity, momentum, energy, and species corresponding to two-dimensional binary alloy solidification are given as

Continuity

$$\frac{\partial}{\partial t}(\rho) + \nabla.(\rho \mathbf{V}) = 0, \tag{1}$$

Momentum

$$\frac{\partial}{\partial t}(\rho u) + \nabla.(\rho \mathbf{V} u) = \nabla.\left(\mu_l \frac{\rho}{\rho_l}\nabla u\right) - \frac{\partial p}{\partial x} - \frac{\mu_l}{K}\frac{\rho}{\rho_l}u - \nabla.\left(\rho \frac{g_s \rho_s}{g_l \rho_l}\mathbf{V}u\right) + \nabla.\left(\mu_l u \nabla\left(\frac{\rho}{\rho_l}\right)\right), \tag{2}$$

$$\frac{\partial}{\partial t}(\rho v) + \nabla.(\rho \mathbf{V} v) = \nabla.\left(\mu_l \frac{\rho}{\rho_l}\nabla v\right) - \frac{\partial p}{\partial y} - \frac{\mu_l}{K}\frac{\rho}{\rho_l}v - \nabla.\left(\rho \frac{g_s \rho_s}{g_l \rho_l}\mathbf{V}v\right) + \nabla.\left(\mu_l v \nabla\left(\frac{\rho}{\rho_l}\right)\right) + \rho^l_{ref} g_a\left[\beta_T(T - T_{ref}) + \beta_C(C_l - C_{ref})\right] \tag{3}$$

Energy

$$\frac{\partial}{\partial t}(\rho T) + \nabla.(\rho \mathbf{V} T) = \nabla.\left(\frac{k}{c_{ps}}\nabla T\right) - \nabla.\left[\left(\frac{c_{pl}}{c_{ps}} - 1\right)\rho \mathbf{V} T\right] - \frac{\partial}{\partial t}\left(\frac{\rho_s g_l h_{sl}}{c_{ps}}\right) - \frac{\partial}{\partial t}\left[g_l\left(\frac{c_{pl}}{c_{ps}} - 1\right)(\rho_l T - \rho_s T_e)\right], \tag{4}$$

Species

$$\frac{\partial}{\partial t}(\rho C) + \nabla.(\rho \mathbf{V} C) = \nabla.(g_l \rho_l D_l \nabla C) + \nabla.[g_l \rho_l D_l \nabla(C_l - C)] - \nabla.[\rho \mathbf{V}(C_l - C)], \tag{5}$$

where g_l and g_s are liquid and solid volume fractions, respectively. Liquid and solid mass fractions are defined as $f_l = g_l \rho_l / \rho$ and

$f_s = g_s\rho_s/\rho$. Mass averaged velocity and volume averaged density are defined as $\mathbf{V} = f_l\mathbf{V}_l + f_s\mathbf{V}_s$, $\rho = g_s\rho_s + g_l\rho_l$, respectively. Both mass and volume fractions follow the relations $f_l + f_s = 1$ and $g_l + g_s = 1$. Third and fourth terms appearing on the right-hand side of u and v momentum conservation Eqs. (2) and (3) represent Darcian damping and inertial forces within the porous mushy region.[41] However, the effect of the inertia terms within the mushy region is much weaker than the Darcian damping term.[41] Fifth term appearing on the right-hand side of u and v momentum conservation Eqs. (2) and (3) is the modifications suggested by Chiang and Tsai[43] and later adapted by Monde *et al.*[44] to include shrinkage induced suction force. Parameter K appearing in the Darcian source term is given as

$$K = K_0\left(\frac{g_l^3 + \varepsilon}{(1 - g_l)^2}\right), \tag{6}$$

where K_0 is permeability constant, and ε is an infinitesimally small numerical value ($\sim 10^{-10}$) to prevent numerical shooting up of Darcian damping term as $g_l \to 0$. The sixth term appearing on the right-hand side of the v momentum Eq. (3) represents the combined thermal and solutal buoyancy force, with β_T and β_C are being defined as thermal and solutal expansion coefficients, respectively.

The energy conservation Eq. (4) is expressed in terms of temperature as the scalar variable.[44,45] The energy conservation Eq. (4) is obtained by substituting mass averaged enthalpy as $h = f_s h_s + f_l h_l$ into volume averaged continuum equation. Here, h_s and h_l are phase enthalpies corresponding to solid and liquid phases, and they are defined as $h_s = c_{ps}T$ and $h_l = (c_{ps} - c_{pl})T_e + h_{sl} + c_{pl}T$, respectively, with T_e and h_{sl} being defined as the eutectic temperature of the binary alloy system and latent heat of phase change, respectively, whereas c_{ps}/c_{pl} is defined as specific heat of solid/liquid phase. The volume averaged thermal conductivity k is defined as $k = g_s k_s + g_l k_l$, where k_s and k_l are the solid and liquid phase thermal conductivity, respectively. The source terms (second, third, and fourth terms) appearing on the right-hand side of energy conservation Eq. (4) are the aftermath of mathematical manipulations of the energy equation to be expressed in terms of temperature as the scalar variable, rather than the average enthalpy.

The species conservation Eq. (5) is represented in terms of mass averaged mixture concentration of the solute C as the scalar variable. Mass averaged solute concentration C is defined as $C = f_s C_s + f_l C_l$, where, C_s and C_l are the local solid and liquid solute concentrations, respectively. For the present formulation, solute diffusivity in solid phase (D_s) is considered to be insignificant as compared to that in liquid phase (D_l), i.e., $D_l \gg D_s$. Therefore, D_s is assigned with zero value implying the absence of solute diffusion in the solid phase. The second and third source terms appearing on the right-hand side of Eq. (5) originate from solute rejection in the melt during the ongoing solidification process. The liquid solute concentration C_l appearing in Eq. (5) is obtained from the mass averaged species concentration and is defined as

$$C_l = \frac{\rho C}{k_p\rho + (1 - k_p)g_l\rho_l}, \tag{7}$$

where k_p is partition coefficient defined as the solute concentration ratio in solid and liquid phases ($k_p = C_s/C_l$). Partition coefficient k_p is obtained from the equilibrium phase diagram with the assumption of the slopes of solidus and liquidus lines to be constant. Although the estimation of C_l from Eq. (7) looks quite straightforward, we should be careful while using the same for calculating solute concentration in the liquid phase. The maximum obtainable solute concentration in the melt is restricted by eutectic concentration, i.e., the condition $C_l \le C_e$ must prevail in the entire solidification domain. Therefore, any value of $C_l > C_e$ obtained from Eq. (7) must immediately be set to a value $C_l = C_e$ to account for this physical constraint.

III. NUMERICAL APPROACH AND PHYSICAL DOMAIN

The governing Eqs. (1)–(5) are in the standard conservative form as described by Patankar.[46] Each of them contains an unsteady term, a convective term, a diffusion term, and source terms. The standard advection and diffusion terms are discretized using the power-law scheme.[46] The source term involving diffusion namely the second term on the right-hand side of Eq. (5) is discretized by using a central difference scheme. The transient source terms namely the third and fourth terms on the right-hand side of Eq. (4) are discretized by forward difference scheme. Finally, the advection source terms [namely the fourth and fifth terms on the right-hand side of Eqs. (2) and (3), the second term on the right-hand side of Eq. (4), and the third term on the right-hand side of Eq. (5)] are discretized by using the first-order upwind scheme. The second-order linear upwind difference scheme (LUDS)[47] is also used as an alternative to the first-order upwind scheme for the discretization of the advection source terms to test the accuracy of the first-order upwind scheme. However, a comparison of the results obtained from these two schemes did not manifest a significant difference. The execution of LUDS being computationally expensive, the majority of the results presented here are obtained by using the first-order upwind scheme to discretize source terms involving advection in momentum, energy, and species conservation equations [Eqs. (2)–(5)]. The numerical procedure is carried out by calculating the flow field using the Semi-Implicit Method for Pressure-Linked Equations Revised (SIMPLER) algorithm to begin with. Once the flow field is obtained, the solution of the temperature and species field follows. The solution of flow, temperature, and species field are then followed by the evaluation of the local liquid volume fraction using a numerical approach originally implemented by Voller and Prakash[48] and later modified by Chakraborty[45] and Monde *et al.*[44] to address different c_p values in solid and liquid phases and shrinkage induced flow. This volume fraction updating scheme[44,45,48] allows us to track the distinct interfaces existing between solid, mushy, and liquid regions in a fixed grid framework. The procedure is repeated for each time step until the flow field and scalar quantities T, C, and g_l satisfies the convergence criteria of 10^{-5}. Since the magnitude of the velocity components is of the order of 10^{-3} m, relative error is considered for the convergence criteria while estimating the flow field. For rest of the scalar parameters convergence criterion are based on absolute error. A line-by-line tri-diagonal matrix algorithm (TDMA) is used to solve the discretized algebraic equations iteratively.

The numerical scheme to update the liquid volume fraction g_l is obtained by the method proposed by Monde *et al.*[44] The scheme involves discretization of the energy conservation Eq. (4) using the finite volume method and obtaining the expressions for two consecutive iteration steps [nth and $(n+1)$th iterations steps]. The expression for $(n+1)$th iteration step is then subtracted from the expression obtained for nth iteration step and rearranged with suitable

assumptions to attain a formulation that relates liquid volume fractions at $(n+1)$th iteration step with the same at nth iteration step as follows:

$$gl_P^{n+1} = gl_P^n + \lambda \frac{\left[B_P \rho_l gl_P^n + a_P^0\right]\left(T_P^n - T_P^{n+1}\right)}{A_P + B_P\left(\rho_l T_P^{n+1} - \rho_s T_e\right)}. \quad (8)$$

In Eq. (8), λ represents a suitable under-relaxation factor, subscript P represents the grid point, and superscript 0 denotes previous time step. A_P, B_P, and a_P^0 appearing in Eq. (8) are given as follows:[46]

$$A_P = \frac{\rho_s h_{sl}}{c_{ps}} \frac{\Delta x \Delta y}{\Delta t}; \quad B_P = \left(\frac{c_{pl}}{c_{ps}} - 1\right) \frac{\Delta x \Delta y}{\Delta t}; \quad a_P^0 = \frac{\rho_p^0 \Delta x \Delta y}{\Delta t}. \quad (9)$$

Since solidification in an elementary control volume can only be achieved when the local temperature of the control volume reaches the liquidus temperature T_{liq} corresponding to the local liquid solute concentration C_l, the value of T_P^{n+1} appearing in Eq. (8) is set to $T_P^{n+1} = T_{liq}$. Thus, the final expression for the liquid volume fraction updating scheme corresponding to binary alloy solidification is obtained as follows:

$$gl_P^{n+1} = gl_P^n + \lambda \frac{\left[B_P \rho_l gl_P^n + a_P^0\right]\left(T_P^n - T_{liq}\right)}{A_P + B_P(\rho_l T_{liq} - \rho_s T_e)}. \quad (10)$$

The governing equations Eqs. (1)–(5) are valid for the entire solidification domain consisting of solid, mushy, and liquid phases; thus, the necessity to track the shape and scale of each region is redundant, rendering the numerical scheme to be a fixed grid-based approach.

Figure 1 represents the schematic of the physical domain of interest consisting of a rectangular cavity with a riser opening located at the center of the top boundary. All the boundaries except the bottom surface are subjected to thermal insulation. The bottom surface is maintained at a temperature $T_c < T_e$ to ensure the directional solidification from the bottom. The entire cavity wall is subjected to no-slip boundary condition, while the riser opening at the center of the top wall is subjected to constant pressure (zero gauge pressure) boundary condition. The numerical simulations are performed for the casting domain of height H_C and width W_C ($H_C \times W_C$). Since the domain of interest is symmetric with respect to the vertical central line, we chose to carry out the computations for one of the symmetric halves to reduce total computational time.

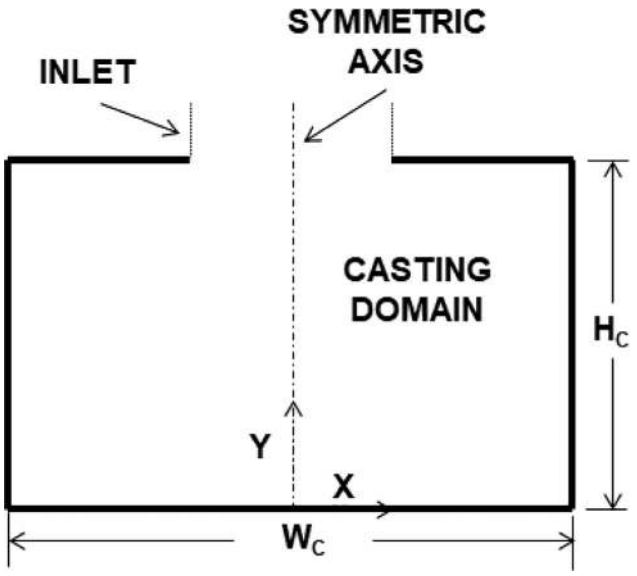

FIG. 1. Schematic of the physical domain of interest.

IV. EFFECT OF GRID AND TIME STEP RESOLUTION ON NUMERICAL PREDICTION OF FRECKLING PHENOMENA

The phenomena of density inversion and freckle formation involving double-diffusive convection during alloy solidification in the bottom cooled configuration is extremely uncertain in nature due to the associated nonlinearity of the problem. Obtaining grid and time step independence for such highly nonlinear problem poses enormous challenge.[40,49,50] In this section, an attempt has been made to address the challenges associated with grid and time step independence.

The solidification domain (Fig. 1) consists of a rectangular cavity of dimension 150×300 mm^2 with an opening of size 40 mm at the center of the top wall. As the computation is performed for one of the symmetric halves (150×150 mm^2), the opening size for the symmetric half is considered to be 20 mm. In order to investigate the effect of grid resolution on simulation results, bottom-up solidification of Al-30 wt. % Mg binary alloy is considered. The alloy is initially at a temperature of 770 K and in pure liquid state. A cold boundary temperature of 720 K is applied at the bottom surface of the cavity. All other surfaces are considered to be perfectly insulated. For all the surfaces, the no-slip boundary condition is implemented for the velocity field. The symmetry plane is subjected to symmetric thermal and velocity boundary conditions. Zero gauge pressure boundary condition is implemented at the top opening for solving momentum conservation Eqs. (2) and (3). The thermo-physical properties of Al–Mg alloy[51–54] is used for this study (Table I).

Analysis is carried out for four different grid resolutions, namely 60×60, 90×90, 120×120, and 150×150 cells, and four different time step resolutions, namely $\Delta T = 0.25$ s, $\Delta T = 0.5$ s, $\Delta T = 0.1$ s, and $\Delta T = 0.05$ s. The number of cells or representative elementary volumes (REV) sharing their boundaries with the top-central opening are 8, 12, 16, and 20, respectively, for these four grid resolutions. For each grid resolution, the numerical simulation is carried out till 100 s to capture the evolution of temperature, velocity, concentration, and liquid–solid volume fraction field. Figure 2 shows the comparison of the Mg concentration field for four different grid resolutions and three different time steps. It is evident from this comparison shown in Figs. 2(a)–2(f) that the dependence of simulation results on grid resolution and time step is unavoidable even with significantly large number of grids and smaller time steps. However, certain distinct features such as locations of plume (channel) formation, number of channels, solid–mushy (y_{sm}), and mushy–liquid (y_{ml}) interface locations showcase reasonably well-behaved similarities with increasing grid resolution. For instance, 90×90, 120×120, and 150×150 grid resolutions with time step $\Delta t = 0.25$ s [Figs. 2(b)–2(d)] showcase fairly similar distribution of channels along with closely matching solid–mushy and mushy–liquid interface locations. The comparison of vertical temperature profile along the symmetry plane at 100 s is shown in Figs. 3(a)

TABLE I. Binary alloy systems used for numerical analysis and their thermo-physical properties.[14,15,51–55]

Properties	Symbol/units	Al-4.1 wt.% Cu	Al-30 wt.% Mg
Thermal conductivity	k (W/mK)	k_l-82.61/k_s-192.49	k_l-90.7/k_s-211
Specific heat	c_p (J/kgK)	c_{pl}-1058.8/c_{ps}-1092.8	c_{pl}-1058.8/c_{ps}-1092.8
Liquid solute diffusivity	D_l (m^2/s)	3×10^{-9}	3×10^{-9}
Density	ρ (kg/m^3)	ρ_l-2400/ρ_s-2650	ρ_l-2070/ρ_s-2190
Latent heat	h_{sl} (J/kg)	397 500	398 000
Dynamic viscosity	μ (kg/ms)	0.003	0.00138
Thermal expansion coefficient	β_T (K^{-1})	4.95×10^{-5}	2.1×10^{-5}
Solutal expansion coefficient	β_C	−0.0092	0.00428
Partition coefficient	k_p	0.17	0.482
Eutectic temperature	T_e (K)	821.2	723
Melting temperature	T_m (K)	933.2	933.2
Eutectic composition	C_e	33.2	36.3
Initial temperature	T_i (K)	970	770
Initial composition	C_0	4.1	30

and 3(b) for varying grid and time step resolutions. The comparisons manifest close resemblance with minimal difference between temperature profiles along the symmetry plane. On the other hand, when the horizontal temperature profile just above the mushy–liquid interface is compared for different grid and time step resolutions [Figs. 3(c) and 3(d)], substantial variations between the temperature profiles can be observed. However, the range of temperature variations is found to be conveniently small (∼3 K). Therefore, we conclude that obtaining simulation results with complete insensitivity to the grid and time step resolution is unattainable for this case study. This observation is in line with several studies reported in literature.[40,49,50] Sung *et al.*[49] studied the grid dependence for freckle formation in 2D with Nickle base superalloy and recommended the grid size relying primary on dendrite arm spacing and solute diffusivity in liquid. Guo and Beckermann[50] performed 3D grid dependence analysis with Pb–Sn alloy and concluded that the finer grid resolution is insufficient to achieve grid independence and is a cause of volatile behavior of freckles formation over initial instabilities. Sajja and Felicelli[40] employed fractional step adaptive meshing, which efficiently and accurately track the freckle formation, but reported two limitations concerning round-off errors and ill-conditioned boundaries. From this endeavor and other existing studies[40,49,50] in the pursuit of achieving grid and time step independence,

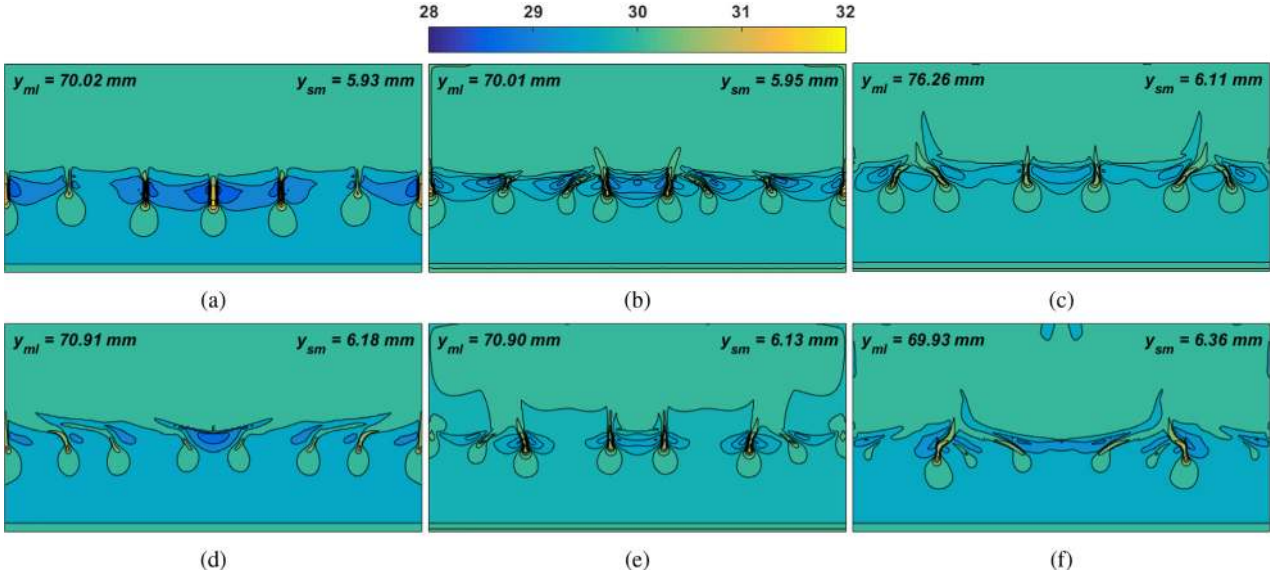

FIG. 2. Mesh sensitivity analysis: Solute composition distribution of Mg after 100 s time interval with varying grid and time step resolutions: (a) 60 × 60 and $\Delta t = 0.25$ s; (b) 90 × 90 and $\Delta t = 0.25$ s; (c) 120 × 120 and $\Delta t = 0.25$ s; (d) 150 × 150 and $\Delta t = 0.25$ s; (e) 150 × 150 and $\Delta t = 0.5$ s; and (f) 150 × 150 $\Delta t = 0.05$ s. y_{ml} and y_{sm} represent mushy–liquid and solid–mushy interface locations, respectively, estimated along symmetric axis.

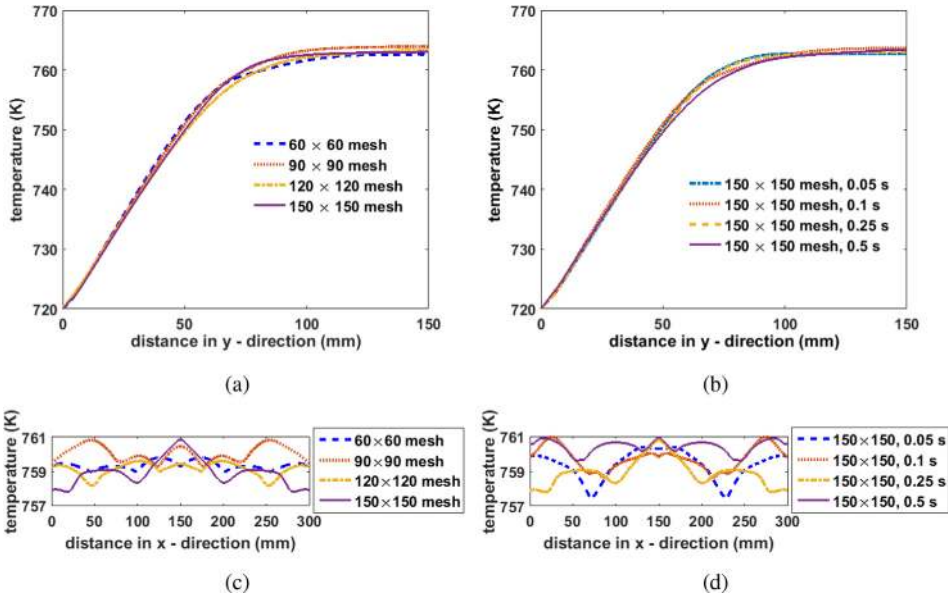

FIG. 3. Comparison of temperature profiles after 100 s time interval (a) along symmetry axis for varying grid resolution and $\Delta t = 0.25$ s; (b) along symmetry axis for varying time step resolution and grid resolution 150×150; (c) along horizontal direction at a distance of $y = 80$ mm from bottom wall for varying grid resolution and $\Delta t = 0.25$ s; and, (d) along horizontal direction at a distance of $y = 80$ mm from bottom wall for varying time step resolution and grid resolution 150×150.

it is clear that achieving complete independence from grid and time resolution will remain unresolved. Since high grid resolution and smaller time steps demand significantly large computational time, we have restricted the grid resolution to 150×150 cells and time step to 0.25 s for all the simulation results discussed in the forthcoming subsections. All the simulations are carried out on an Intel(R) Xenon(R) CPU E5–2650 v4 @ 2.20 GHz computer and, for the 150×150 grid cells, required approximately 24–240 CPU seconds for each 1 s of real-time simulation. The maximum total CPU time required to complete the simulation is approximately 25 h.

V. RESULTS AND DISCUSSION

The bottom-up directional solidification process is instigated once the bottom surface temperature drops down below the liquidus temperature (T_{liq}) of the alloy system (Fig. 1). The domain undergoing solidification is filled with the molten metal at the initial temperature (T_i) above the liquidus temperature (T_{liq}) of the alloy system. A continuous inflow of molten liquid is assumed to be maintained into the domain through the riser opening at the center of the cavity top surface exposed to atmospheric pressure. Numerical analysis of the bottom-up directional binary alloy solidification process is performed for two different alloy systems, namely (i) Al-4.1 wt. % Cu alloy, and (ii) Al-30 wt. % Mg alloy. The first case study corresponding to the solidification of Al-4.1 wt. % Cu alloy is carried out to validate the numerical model by comparing model predictions with existing numerical[14,15] and experimental[56] data. The second case study corresponding to the solidification of Al-30 wt. % Mg alloy pertains to the investigation of freckle formation under the influence of shrinkage induced flow. The thermo-physical properties used for this study are enlisted in Table I.

A. Solidification of Al-4.1 wt. % Cu

The first case study involving bottom-up directional solidification of Al-4.1 wt. % Cu alloy is carried out for validating the proposed numerical model by comparing the model predictions with the numerical[14] and experimental[56] data. The solidification domain consists of a rectangular cavity of dimension 150×20 mm^2. Solidification is promoted by removing heat continuously from the bottom surface by means of circulation of heat transfer fluid between the bottom surface and a chiller maintained at a temperature of 293 K. The convective heat transfer between the bottom wall and chiller is assigned with an effective heat transfer coefficient of $h_c = 837$ W/m^{2}K. All other sides of the domain are assumed to be insulated. The top surface of the melt is considered to be open, allowing melt flow from above, and subjected to atmospheric pressure.[14,15] As the melt starts to solidify unidirectionally from the bottom, the positive temperature gradient in the vertically upward direction gives rise to a stably stratified thermal buoyancy field in the melt domain, eradicating the possibility of attaining thermal buoyancy-driven natural convection. For the chosen alloy system, Aluminum and copper play the role of solvent and solute, respectively. Due to a much lesser solute (Cu) solubility in the solid phase as compared to the liquid phase, solidification of the Al-4.1 wt. % Cu alloy system leads to the rejection of Cu in the melt adjacent to the newly transformed solid phase. Copper, being heavier than aluminum, copper enriched melt adjacent to the newly transformed solid phase also becomes heavier, promoting the accumulation of Copper rich melt in the lower region of the cavity. Once again, heavier solute rejection during liquid to solid phase transition leads to a stably stratified solutal buoyancy field eliminating the existence of solutal buoyancy-driven natural convection in the melt. Therefore, the convection field obtained in the cavity is solely associated with the shrinkage induced effects. The predicted solute concentration distribution and temperature distribution from the present model are compared with the existing numerical prediction[14,15] and are shown in Figs. 4(a) and 4(b), where the values of scalar variables are the mean average in horizontal direction. Formation of inverse solutal segregation (negative slope of solute concentration inside the solid and mushy region) [Fig. 4(a)] is predicted by both the models, and the agreements between the vertical temperature and solute field predicted by these

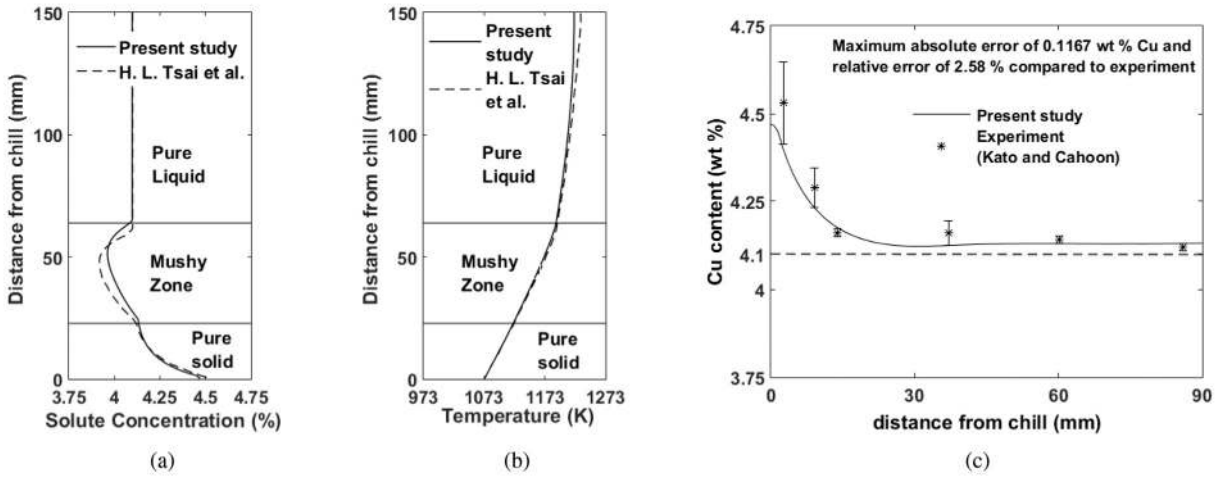

FIG. 4. Comparison of (a) solute distribution and (b) temperature distribution profiles along vertical direction at t = 180 s obtained from the present model and the existing numerical model,[14,15] and (c) comparison of final solidified solute distribution predicted by the present model and obtained from the experiment.[56]

two models are found out to be reasonable. Marginal difference in the results can be observed within the mushy region concerning solute variation due to slight mismatch between mushy–liquid interface location. This slight deviation in interface location also caused a marginal mismatch of temperature profiles in the liquid domain.

Marginal mismatch found during the model validation with existing numerical result compelled us to verify the proposed model against experimental data. Diao and Tsai[14] and Chen and Tsai[15] validated their numerical prediction with experimentally obtained solute distribution in the as cast product of Al-4.1 wt. % Cu alloy reported by Kato and Cahoon.[56] We also compare our model prediction with the experimental results reported by Kato and Cahoon[56] in a similar manner. This comparison is shown in Fig. 4(c). Once again, reasonable agreement is obtained between the model prediction and experimental data within ∼2% error limit.

The reason behind the existence of the negative solutal segregation in the mushy region is worth explaining. From the inception of the solidification process adjacent to the bottom surface, the melt surrounding the newly transformed solid-phase gets enriched with heavier solute (Copper) concentration causing a depression of liquidus temperature of this solute-rich melt. The depression of local liquidus temperature hinders the liquid to solid phase transformation of this liquid-rich melt at the bottom of the cavity any farther. However, the regions above the solute-rich melt having a leaner solute (Copper) concentration and higher liquidus temperature starts solidifying as the local temperature decreases sufficiently, promoting farther rejection of heavier solute (Copper). The solute-rich, heavy melt thus produced in the mushy region keeps leaching in the downward direction, making the cavity bottom filled with liquid melt with ever-increasing solute concentration delaying the solidification process in that region farther. However, the region adjacent to the cold bottom surface being the coldest region in the cavity, complete solidification is eventually attained as the local temperature approaches the eutectic point. The combined effect of the heavier melt leaching in the mushy region and the shrinkage induced flow allows the solute lean melt from the pure liquid region above to percolate inside the mushy region. The mushy region already contains a dispersed solid fraction within it, and the solute content of this dispersed solid phase is much below the nominal solute (copper) concentration (C_0) of the melt. The entry of solute (copper) lean melt from the pure liquid region from above causes an overall depression of solute (copper) concentration (given by $C = f_s C_s + f_l C_l$) below C_0 for a portion of the mushy region defined as negative segregation. At the advent of solidification, this negative segregation is confined only to the uppermost section of the mushy zone. However, with the progress in the solidification process, as the solid–mushy and mushy–liquid interface keeps moving in the upward direction, the region of negative segregation gradually engulfs the entire mushy region.

The reasonable match obtained from the validation of the present model concerning solute concentration and temperature distribution (Fig. 4) establishes the robustness and reliability of the present model. The confidence in the present model being justified by this validation, we next endeavor to implement the model to investigate the binary alloy solidification associated with freckle formation under the combined influence of solutal convection and shrinkage induced flow in the next subsection.

B. Solidification of Al-30 wt. % Mg

For the case study associated with freckle formation under the combined influence of solutal convection and shrinkage induced flow, we have chosen Al-30 wt. % Mg as the model binary alloy. For this binary alloy system, aluminum assumes the role of solvent, and magnesium plays the role of solute. The motivation to choose Al-30 wt. % Mg as the model binary system for this study arises from the similarity of the phase diagram of Al–Mg alloy with NH_4Cl-H_2O binary system, which is one of the most common model binary system deployed to study freckle formation phenomena.[19,21,22,28–31] However, NH_4Cl-H_2O binary system being subjected to volume expansion instead of shrinkage during liquid–solid phase transition process makes such a well-studied system invalid for our current study involving shrinkage

induced flow. For all the reported case studies involving freckling phenomena during the solidification of NH_4Cl-H_2O binary system, the initial concentration (C_0) is chosen close to the eutectic composition.[19,21,22,28–31] Apart from this, the Al–Mg alloy system having a large shrinkage ratio (ρ_s/ρ_l) is ideal for promoting shrinkage induce flow during the solidification process. Al–Si is another potential binary alloy system that we explored for this study considering the large value of shrinkage ratio (ρ_s/ρ_l).[57] However, owing to the smaller difference between the solubility in solid and liquid phases along with a much smaller value of solutal expansion coefficient β_C, Al–Si binary system is less prone to promote significant solutal instability leading to the formation of freckles.[58] Also, Al–Mg being a commonly used alloy system for various industrial applications, we chose this system as our model binary alloy. It is pertinent to mention here that the effect of micro-structure on permeability is not considered for the current study. Since the permeability linked with micro-structure in the mushy zone plays a key role in defining the freckling phenomena,[11] the exclusion of the micro-structure effect in the present model is one of the major limitations of this study. However, the flow physics captured by this study is expected to be valid whenever the micro-structure in the mushy region is conducive of promoting freckling phenomena. Hence, the results obtained from the study considering Al-30 wt. % Mg alloy as the model binary system can be considered to be consistent without losing any generality; and the physical understanding of the phenomena is equally applicable to any other binary system with favorable micro-structure in the mushy zone to promote freckle formation under the influence of shrinkage induced flow.

For the bottom cooling configuration, liquid to solid phase transition ensues from the bottom section of the cavity, causing rejection of lighter solute (magnesium) in the adjacent melt. The presence of excess lighter solute (magnesium) in the melt at the lower region of the cavity promotes instability of the solutal buoyancy field within the melt. When the instability of the solutal buoyancy field becomes strong enough to overcome the stably stratified thermal buoyancy field, free convection in the form of plumes ensues, causing the formation of channels in the mushy region.[11,12] For the present study, the alloy

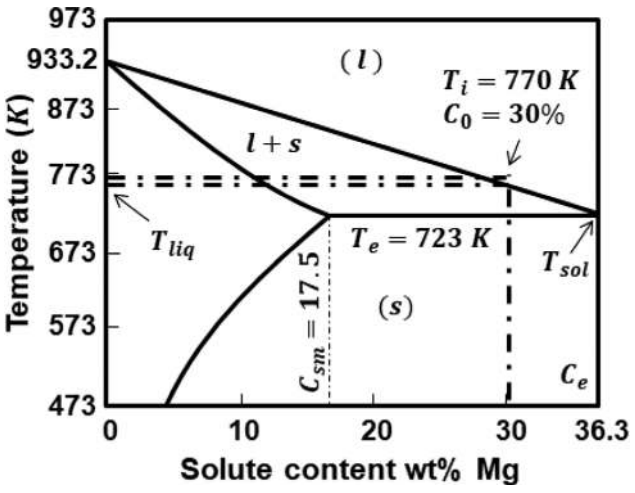

FIG. 5. Al (solvent)-Mg (solute) phase diagram till eutectic composition.

composition is initially maintained at a temperature $T_i = 770$ K (Fig. 5) which is approximately 10 K above the liquidus temperature corresponding to nominal magnesium composition ($C_0 = 30\%$). Solidification is attained by maintaining the bottom wall temperature below eutectic temperature (T_e at time $t > 0$ s). The initial set of studies are performed by maintaining the bottom wall temperature 3 K below eutectic temperature ($T_e = 723$ K). The rejected solute (Mg) in the melt being lighter during the growth of solid front from the bottom, the solutal and thermal buoyancy fields oppose each other. While the effect of lighter solute rejection during solidification at the cavity bottom attributes to the density reduction of the local melt, the effect of low temperature (associated with the positive temperature gradient in the upward direction) on density is reverse at the cavity bottom.[11,12] One way to ensure density inversion at the cavity bottom is to enhance the instability of the solutal buoyancy field while suppressing the stable stratification effect of the thermal buoyancy field. The suppression of the thermal buoyancy effect can be attained by setting up an overall small temperature difference across the melt domain.

1. Effect of shrinkage induced flow on freckle formation

In the present subsection, the effect of shrinkage induced flow on freckle formation is analyzed. Cavity geometry, boundary conditions, and initial condition are considered to be the same as the physical domain description in Sec. IV involving grid and time step independence study. Figures 6–8 represent the velocity field, liquid fraction and stream function, and species distribution within the rectangular cavity domain at different time intervals during the ongoing solidification process. As is evident from Figs. 6(a)–8(a), the melt convection in the cavity is predominantly developed due to the shrinkage effect at the initial stage of solidification (at $t = 20$ s), and density inversion due to the instability of solutal buoyancy field is absent during this stage. At the initial stage of solidification, volumetric shrinkage due to the solidification causes melt inflow into the cavity through the opening located at the top surface of the cavity giving rise to the circulation of melt adjacent to the opening. However, owing to the resistance posed by the stably stratified thermal buoyancy field, the incoming flow through the cavity opening cannot penetrate deeper into the cavity, and rather rerouted along the lateral direction having lesser flow resistance. Thus, at the initial stage of solidification, the interaction between the shrinkage induced flow and stably stratified thermal buoyancy field manifests a counter-intuitive flow reversal phenomena akin to the observations made by Monde *et al.*[44] during the study involving bottom-up solidification of pure substance in a cavity with a central riser. As the solidification process progresses in time, solutal instability sets in near the mushy–liquid interface [Figs. 6(b)–8(b)] due to the rejection of excess lighter solute (Mg) in the melt caused by liquid to solid phase transition. The advent of solutal instability also leads to the onset of freckle formations in the mushy region. Coupled interaction between the shrinkage induced flow and solutal instability gives rise to complicated flow evolution in the melt region [Figs. 6(b) and 6(c)] defining shape and orientation of the channels within the mushy region [Figs. 7(b) and 7(c)]. The slanted orientation of channels shown in Figs. 7(c) and 7(d) can be attributed to this coupled interaction. As is evident from Figs. 8(c) and 8(d), the evolution of macro-segregation or species distribution is strongly influenced by the flow field. All the channel locations are characterized by positive segregation ($C > C_0$),

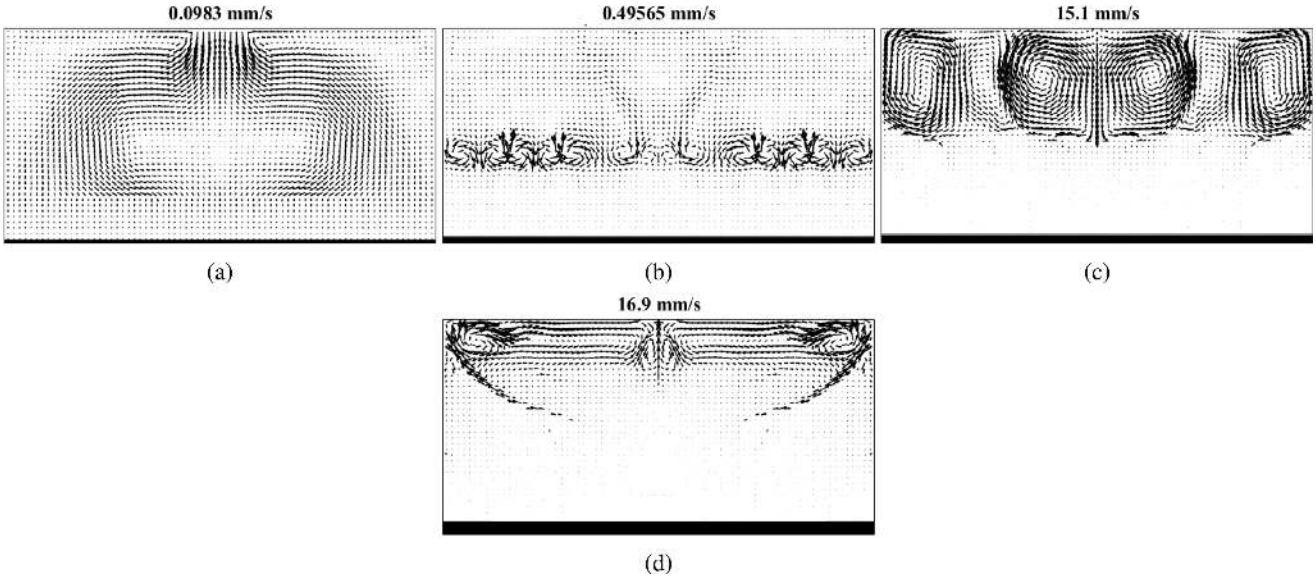

FIG. 6. Numerically predicted velocity field in the rectangular domain at different time intervals: (a) t = 20 s (b) t = 60 s, (c) t = 100 s, and (d) t = 200 s. Magnitude of the maximum velocity within the domain is mentioned at the top of the individual figure.

while all the surrounding mushy regions are having negative segregation ($C < C_0$). With the further progress of the solidification process, the strength of the plumes gradually diminishes owing to the ever reducing height of the melt zone and natural closure of the channel openings into the melt region due to their slanted orientations. As the growth of the mushy region extends to approach the upper wall of the cavity, shrinkage induced flow reclaims its domination in the pure liquid and mushy region in the presence of very weak solutal influence [Figs. 6(d) and 7(d)]. The effect of shrinkage induced flow on macro-segregation is distinctively manifested by a concentration distribution that resembles a stag-horn structure spreading symmetrically on both sides and centered around the symmetric plane [Fig. 8(d)].

2. Effect of inlet opening size on macro-segregation during freckle formation

The intensity of the shrinkage induced flow is expected to have a significant influence on the evolution of freckle orientation and

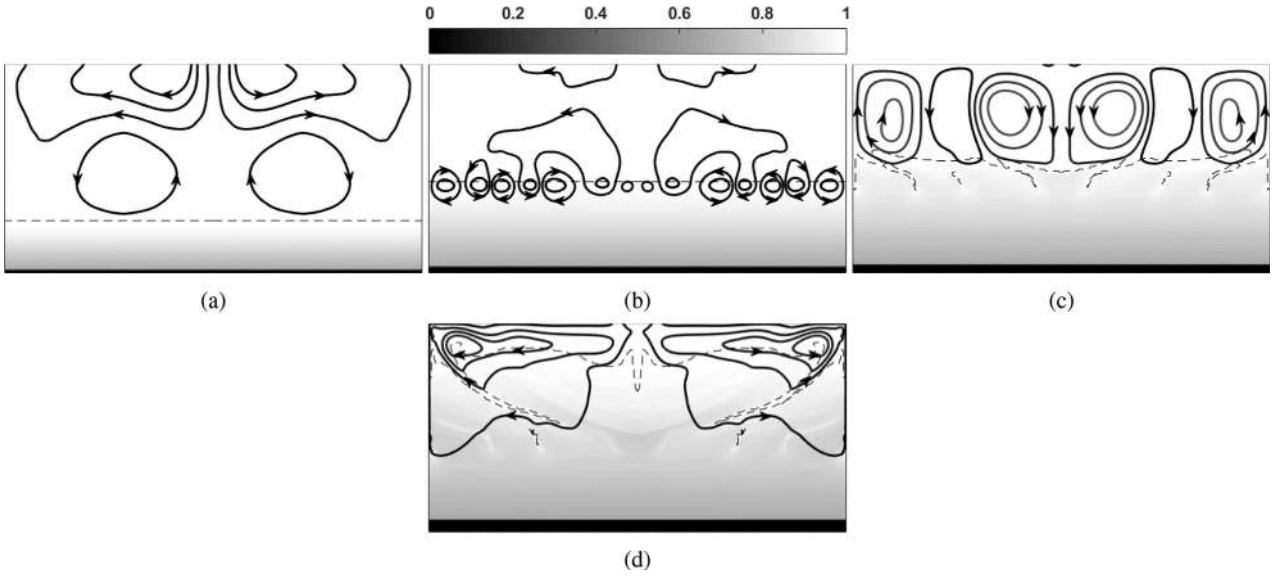

FIG. 7. Numerically predicted liquid fraction and stream function in the rectangular domain at different time intervals: (a) t = 20 s (b) t = 60 s, (c) t = 100 s, and (d) t = 200 s. Dashed lines denote the mushy–liquid interface.

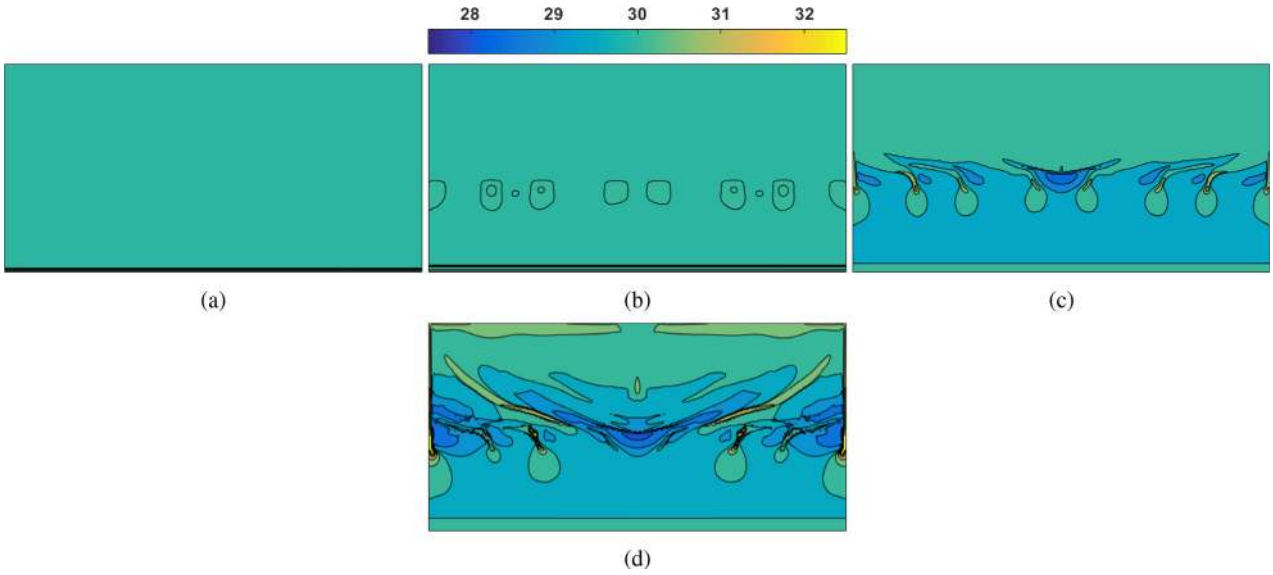

FIG. 8. Numerically predicted solute (Mg) distribution in the rectangular domain at different time intervals: (a) t = 20 s (b) t = 60 s, (c) t = 100 s, and (d) t = 200 s.

macro-segregation. The prediction of the macro-segregation in the final cast product is of imminent interest in many manufacturing applications. Therefore, we endeavor to study the effect of shrinkage induced flow intensity on the final macro-segregation pattern in the cast product. The intensity of the shrinkage induced flow is highly dependent on the size of the opening for melt inflow into the cavity and the boundary condition at the bottom surface. In the present subsection, the study involves varying shrinkage induced flow intensity by means of varying the opening size, while the cold bottom boundary is maintained at the same constant temperature. The second part of the study involves varying cold boundary temperature for a fixed inlet opening size and will be discussed in the subsequent section.

For the varying opening size analysis, simulations are performed with six different inlet openings at the center of the top surface of the cavity, namely 16 mm, 30 mm, 40 mm, 60 mm, 150 mm, and fully open (300 mm). For all these cavity openings, the bottom wall temperature is maintained at 700 K. All the geometric parameters and initial condition, and other boundary conditions are considered to be the same as those discussed in the preceding subsections. Unlike the case studies discussed in the preceding subsections (with bottom surface temperature 3 K below the eutectic temperature), the bottom wall temperature is purposefully chosen to be at a lower value (23 K below the eutectic temperature) to expedite the solidification process and to obtain faster completion of the solidification process in the cavity. Figures 9 and 10 show the predicted concentration and velocity fields, respectively, for different inlet size openings obtained after the time interval 80 s. The simulation results indicate that the opening size has negligible influence over the onset of solutal instability and freckle formation, and for all different opening sizes, the solutal instability initiates almost after the same time interval. However, once the convection in the form of plumes sets in, the concentration distribution and flow field in the melt domain is significantly sensitive to the opening size (Figs. 9 and 10). For smaller openings, although the shrinkage induced flow intensity is high along the symmetry line, most of the flow interactions with this incoming flow are restricted only with the nearest pair of neighboring plumes adjacent to the symmetry line [Figs. 10(a) and 10(b)]. As the opening size increases, the intensity of shrinkage induced flow reduces considerably. However, the zone of flow interaction is not restricted to a domain just adjacent to the symmetry line only. As a result, the weak incoming flow field through the opening interacts with more number of upcoming plumes resulting in significant alteration of the flow field at the upper half of the cavity [Figs. 10(c)–10(e)]. When the entire upper surface of the melt is exposed to inflow, the intensity of shrinkage induced flow becomes extremely weak, and plume convection due to solutal instability dominates in the melt region [Fig. 10(f)]. Although the shrinkage induced flow intensity is extremely weak for the completely open-top configuration, the effect of flow interaction is still perceivable from Fig. 10(f). Strong plumes moving in the upward direction around the cavity symmetry lines pose a strong resistance for the shrinkage induced flow to penetrate inside the cavity through the central portion of the opening. As a result, most of the shrinkage induced incoming melt through the opening is coerced to enter the cavity through the two corner sections of the opening. The effect of incoming melt flow through the opening corners is to suppress the plume formations in those regions and bending of stronger plumes at the two extremities toward the central region. Thus, the effect of opening size on the plume and channel formation can be comprehensively summarized as follows: (i) for small opening size, the shrinkage induced flow interacts mostly with the pair of immediately neighboring plumes adjacent to the symmetry line [Figs. 10(a) and 10(b)]; (ii) for moderate opening size, the effect of shrinkage induced flow expands laterally from the centerline, and more number of neighboring plumes distributed around the central line interact with the incoming flow [Figs. 10(c)–10(e)]; and finally, (iii) for very large opening size, the interaction of shrinkage induced flow is negligibly small with the plumes generated around the central symmetry line but having a significant contribution in the suppression of the corner plumes [Fig. 10(f)].

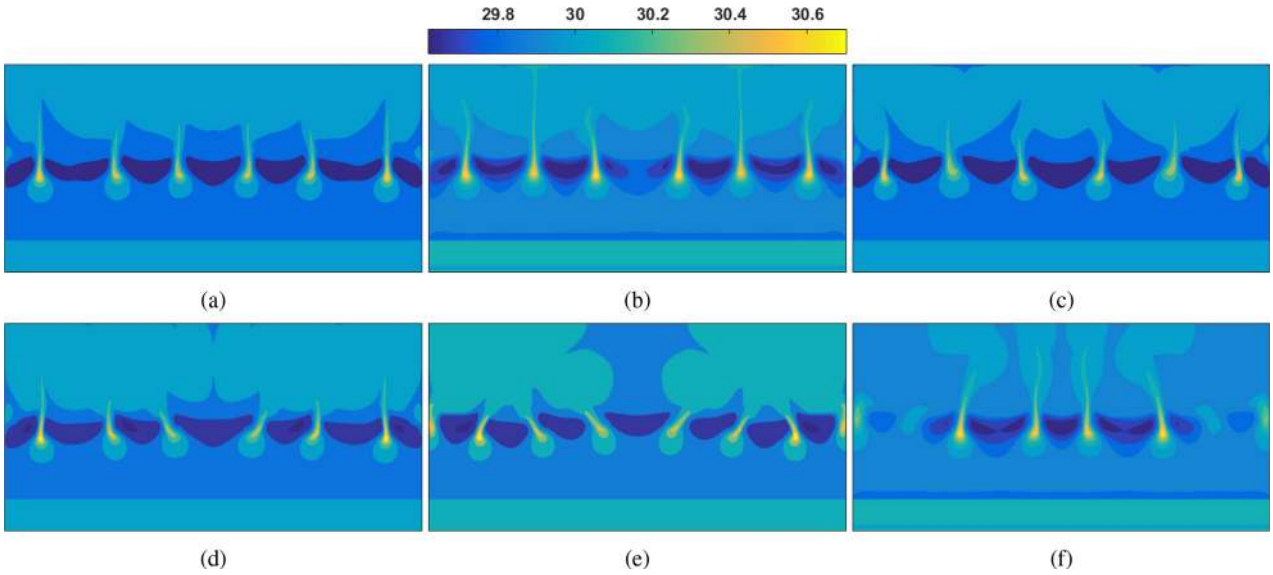

FIG. 9. Numerically predicted solute (Mg) distribution in the rectangular domain for different inlet openings sizes at $t = 80$ s: (a) 16 mm, (b) 30 mm, (c) 40 mm, (d) 60 mm, (e) 150 mm, and (f) 300 mm.

The plumes observed in this numerical study are similar to the results reported in literature.[30,49,59] The observed channels are purely developed due to solutal instability and has a point source of order 10^{-4} m, which have been perceived both numerically[30,59] and experimentally.[31] However, the classic plume structures formed by localized heating are quite different from the present plume structure. These classic plumes are generally observed with periodic puff and bulge that corresponds to instability of lapping flow.[60,61] In thermally driven plumes, the surrounding ambient is at a temperature lower than the heating source placed at the bottom. Due to the thermal instability, buoyancy force directs the lighter fluid present near the hot source in upward direction. The disturbance observed on the surface of thermally driven plume is developed due to dynamic interaction of surrounding fluid with the plume. Particularly when the plume has a point source, the disturbance augments as the density difference between the surrounding and plume reduces[62] leading to sinusoidal disturbance. In this study, plume sources are similar to point source and caused by marginal change in solute concentration. Therefore, the

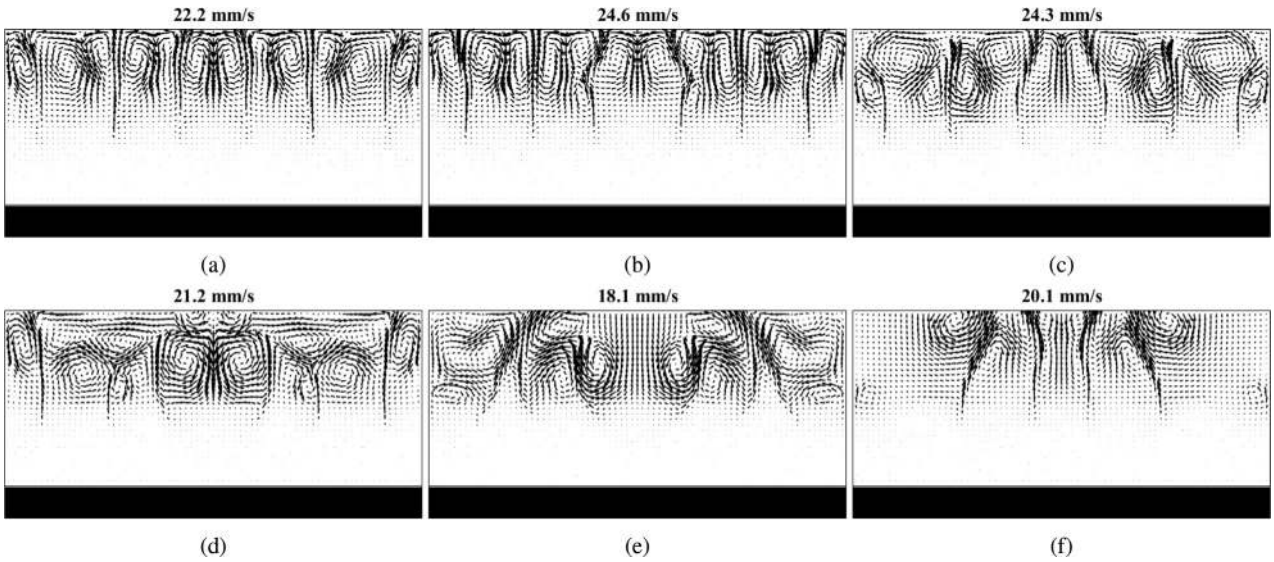

FIG. 10. Numerically predicted velocity field in the rectangular domain for different inlet openings sizes at $t = 80$ s: (a) 16 mm, (b) 30 mm, (c) 40 mm, (d) 60 mm, (e) 150 mm, and (f) 300 mm. Magnitude of the maximum velocity within the domain is mentioned at the top of the individual figure.

situation is conducive of promoting sinusoidal disturbance rather than periodic puffing and bulging phenomena.

Further, Figs. 11(a)–11(f) show a comparison of the final macro-segregation after the completion of the solidification process in the cavity for different inlet opening sizes. It is evident from these results that macro-segregation and freckles formation has a strong dependence on the evolving velocity distribution owing to the interaction between shrinkage induced flow and solutal instability. The final macro-segregation pattern around the symmetry field distinctively resembles a wide variety of ram-head pattern [Figs. 11(a)–11(f)]. In an earlier instance [Fig. 8(d)], at an intermediate stage of solidification in the cavity with an opening size of 40 mm and bottom surface temperature 720 K, we came across a similar (stag-horn) segregation pattern. For the cases with smaller openings, the severe solute lean regions are observed adjacent to the opening at the top surface owing to the inflow of liquid melt with a nominal composition (C_0) into the mushy regions in those locations [Figs. 11(a)–11(d)]. On the other hand, for large opening sizes [Fig. 11(e)], these severely solute lean locations are shifted toward the opening corner sections. For a fully open top surface, mild entrainment of severely negative segregation is observed at the central and lateral locations adjacent to the open surface [Fig. 11(f)]. This mild entrainment of severely solute lean regions can be attributed directly to the very low intensity of shrinkage induced flow for this particular case. To substantiate the significance of shrinkage effect over the channel formation and macro-segregation, simulation is also performed without considering the shrinkage induced flow, and the macro-segregation obtained after the completion of the solidification process is depicted in Fig. 11(g) for comparison. As is evident from this comparison, the macro-segregation pattern without considering shrinkage induced flow is found out to be distinctively different from those involving the influence of shrinkage induced flow.

3. Effect of cold boundary temperature on macro-segregation

Next, we analyze the effect of cold boundary temperature on the final macro-segregation. For this particular set of case studies, the opening size at the center of the cavity top surface is kept fixed at 40 mm. Final macro-segregation patterns for three different cold boundary temperatures, namely 700 K, 623 K, and 523 K are presented in Figs. 12(a)–12(c). In order to show the effect of cold boundary temperature on macro-segregation, we have purposefully chosen these cold boundary temperatures representing moderate, low, and very low cold boundary ($T_c = 700$K, 623 K, and 523 K, respectively) at the bottom surface. Only when the unstable solutal buoyancy field overpowers the stably stratified thermal buoyancy field in the melt region, the solutal instability sets in, causing the onset of plume formation. Therefore, the onset of plume formation is essentially decided by the

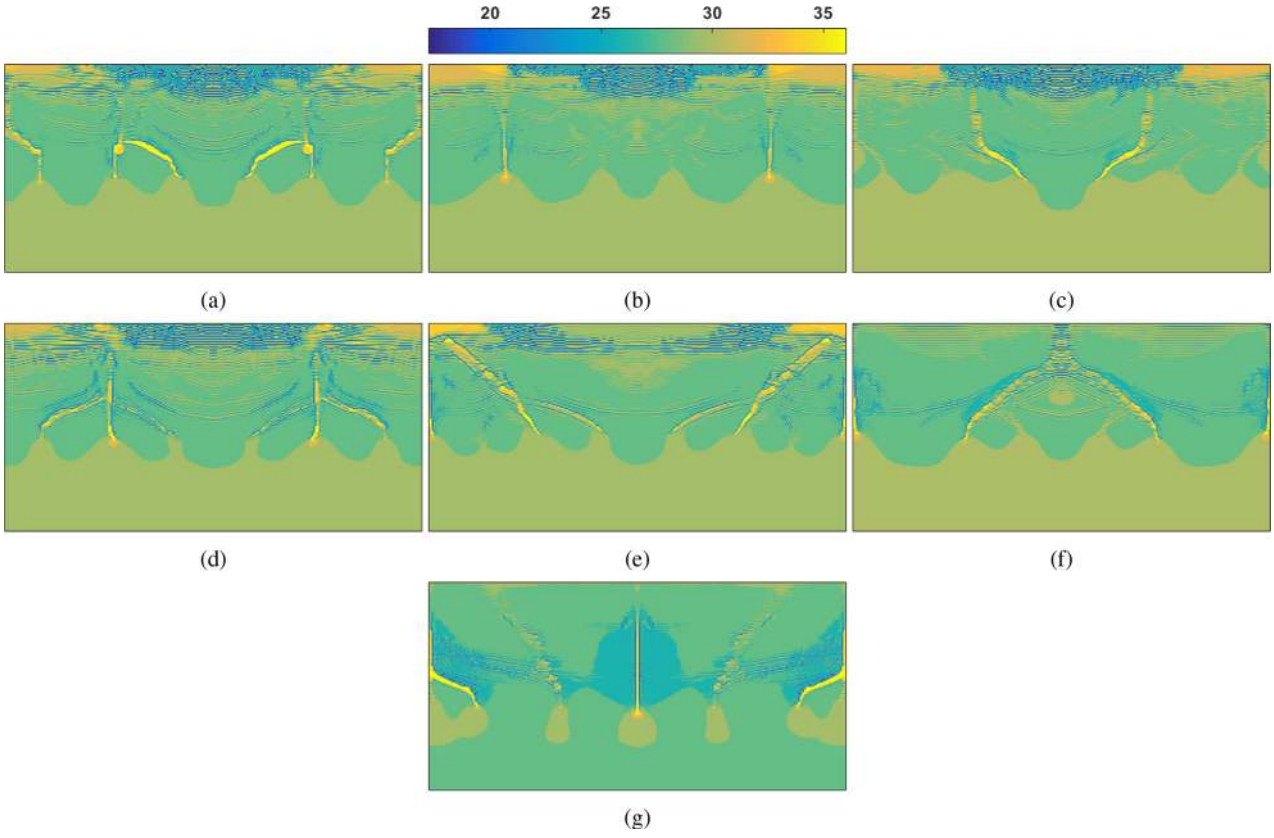

FIG. 11. Numerically predicted macro-segregation after the completion of the solidification process in the cavity for different inlet openings sizes: (a) 16 mm, (b) 30 mm, (c) 40 mm, (d) 60 mm, (e) 150 mm, (f) 300 mm, and (g) a case without considering the effect of shrinkage ($\rho_s = \rho_l = 2190$ kg/m^3) for 300 mm opening size.

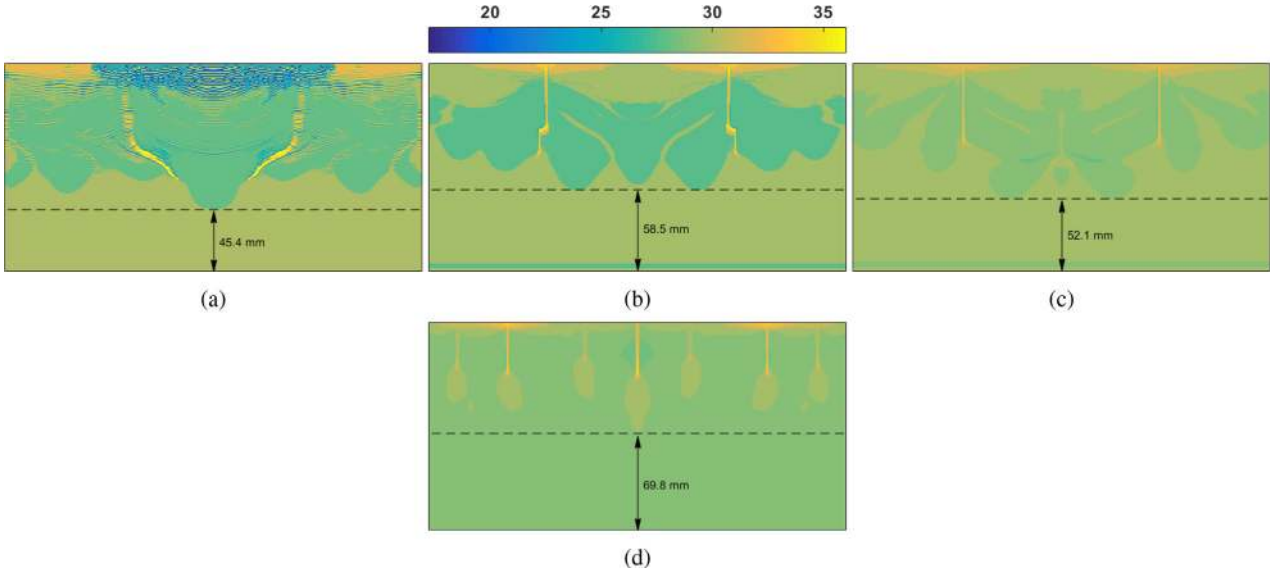

FIG. 12. Numerically predicted macro-segregation after the completion of the solidification process in the cavity for varying cold boundary temperatures: (a) $T_c = 700$ K, (b) $T_c = 623$ K, (c) $T_c = 523$ K, and, (d) a case without considering the effect of shrinkage ($\rho_s = \rho_l = 2190$ kg/m^3) for $T_c = 523$ K.

temperature, and solutal gradients along the vertical direction in pure melt region bounded at its lower end by the liquid–mushy interface. The growth rate of the mushy–liquid interface is directly related to the extent of cooling at the bottom surface. The lower the cold boundary at the bottom surface faster is the growth rate of the mushy–liquid interface and vice versa. When we compare the final macro-segregation patterns for 700 K and 623 K cooling at the bottom surface [Figs. 12(a) and 12(b)], we find that the effect of channel formations are confined to a narrower thickness band at the upper portions of the cavity for the lower cooling. The net effect of lowering the cold surface temperature at the bottom is to shift the freckles formation in the upward direction to a small extent. The lowermost extent of ram-head protrusion [Figs. 12(a) and 12(b)] of the macro-segregation pattern signifies the onset of solutal instability. In terms of the growth rate of the mushy–liquid interface, the mushy–liquid interface moves further up for low cold temperature (623 K) as compared to moderate temperature (700 K) before solutal instability sets in. However, this upward shifting trend of freckles formation does not prevail as we bring down the cold temperature further down till we attain a very low cold temperature of 523 K [Fig. 12(c)]. Not only the macro-segregation pattern for very low cold temperature [Fig. 12(c)] shows a distinct deviation from those depicted for moderate and low cold temperature [Figs. 12(a) and 12(b)], the effect of freckles formation is also spread over a broader thickness band at the upper portion of the cavity, indicating the onset of solutal instability at an early stage of solidification process. This early onset of solutal instability for very low cold temperature is truly intriguing and demands a feasible explanation. The very first idea that propels us to justify this highly nonintuitive feature is that it must be something to do with the effect of shrinkage induced flow. To confirm this notion, we performed another simulation considering the same very low cold temperature (523 K) for the same system without considering the shrinkage effect and compared the macro-segregation [Fig. 12(d)]. The comparison between Figs. 12(c) and 12(d) clearly confirms that the shrinkage induced flow indeed plays a key role in instigating early onset of freckle formation for very low cold temperature.

The depth of the freckle-linked macro-segregation band is distinctively narrower when shrinkage induced flow is not taken into account [Figs. 12(c) and 12(d)]. The early onset of solutal instability is attributed to the perturbation of the metastable solutal buoyancy field adjacent to the mushy–liquid interface by the shrinkage induced flow current coming down from the riser opening. The strength of shrinkage induced downward flow current is highly dependent on the extent of cooling at the bottom surface. The lower the cold temperature, the faster is the solidification rate, and the stronger is flow current entering the cavity through the central opening at the top surface to compensate for the reduced volume due to solidification. When the cold temperature is substantially low, the incoming shrinkage induced flow penetrates deep enough into the melt domain to perturb the metastable solutal buoyancy field adjacent to the mushy–liquid interface. This perturbation causes the solutal instability to set in just around the line of symmetry. The metastable buoyancy field adjacent to the mushy–liquid interface is characterized by the presence of distinct solute-rich zones along with this interface. The horizontal distribution of solute just above the mushy–liquid interface clearly demonstrates these local solute-rich zones with distinct peaks of solute concentration (Fig. 13). These solute-rich zones can be directly identified to be the possible plume sites. The coexistence of such solute concentration peaks along with positive peaks of vertical velocity components (of the range of ~0.8–1.5 mm/s) is identified as the onset of solutal instability (Fig. 13). An example for the same is presented in Fig. 13, where onset is obtained for the case with 40 mm opening and cooling of 700 K. Figures 14(a) and 14(b) shows the onset of this solutal instability adjacent to the central plane of symmetry for 523 K cold boundary at the bottom surface. With the passage of time, this instability around the central symmetry line propagates in the lateral direction establishing

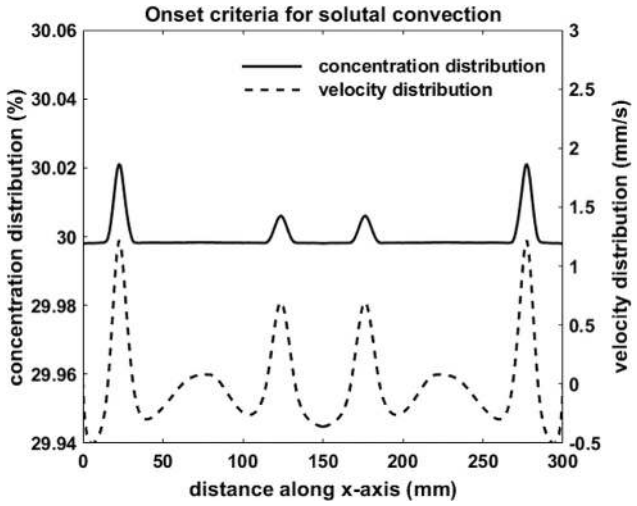

FIG. 13. Onset criteria defined by coexisting peaks in horizontal concentration distribution and vertical velocity component distribution near the metastable buoyancy field adjacent to the mushy–liquid interface for the case study with 40 mm inlet opening size and 700 K cold boundary.

new plume formation sites away from the central symmetry line [Figs. 14(c) and 14(d)]. To emphasize the significance of the shrinkage induced flow strength as the major driving factor of the early onset of solutal instability, the flow pattern [Fig. 14(a)] obtained during the onset of plume formation for 523 K cold boundary at the bottom surface is compared with those obtained for 623 K and 700 K cooling [Figs. 14(e) and 14(f)]. Figures 14(e) and 14(f) clearly show that unlike 523 K cold boundary, solutal instability simultaneously sets in at several locations along with the mushy–liquid interface. However, the interspace between the subsequent plume onset locations is much smaller for 623 K cold boundary [Fig. 14(e)] as compared to 700 K cold boundary [Fig. 14(f)]. The key observations from this study can be consolidated as follows: (i) larger cooling promotes stronger shrinkage induced flow current to penetrate deeper into the melt region adjacent to the central symmetry plane, (ii) the stronger the shrinkage induced flow current, the narrower is the region of solutal instability around the central plane of symmetry with smaller interspace between subsequent plume locations, and (iii) substantially large cooling by lowering the cold temperature triggers the early onset of solutal instability both in terms of timescale as well as the height of mushy–liquid interface.

Another interesting fact revealed by the comparison of macrosegregation patterns presented by Figs. 12(a)–12(c) is associated with the severity of composition distribution in terms of the difference between the maximum and minimum concentration of Mg. A close look at the color bar representing the solute concentration scale in conjunction with the color-map representation of Mg concentration field in Fig. 12 clearly shows that moderate cooling at the bottom surface ($T_c = 700$ K) gives rise to a much severe segregation denoted by $(C_{max} - C_{min}) \sim 19\%$ [Fig. 12(a)]. For $T_c = 623$ K [Fig. 12(b)], $(C_{max} - C_{min})$ value is much smaller (~12%) and for $T_c = 523\,K$ [Fig. 12(c)], $(C_{max} - C_{min})$ value is even smaller (~6%). This ever-decreasing $(C_{max} - C_{min})$ value with progressively lower cold temperature can be directly connected to the relative thickness of the mushy regions. For low cold temperature at the bottom surface, the pure liquid and pure solid region are separated by a thinner layer of the mushy region. On the other hand, a moderate temperature at the bottom surface gives rise to a comparatively thicker mushy layer separating the pure liquid and solid phases. It is the growth rate of the pure solid region that dictates the inflow of melt with a nominal composition

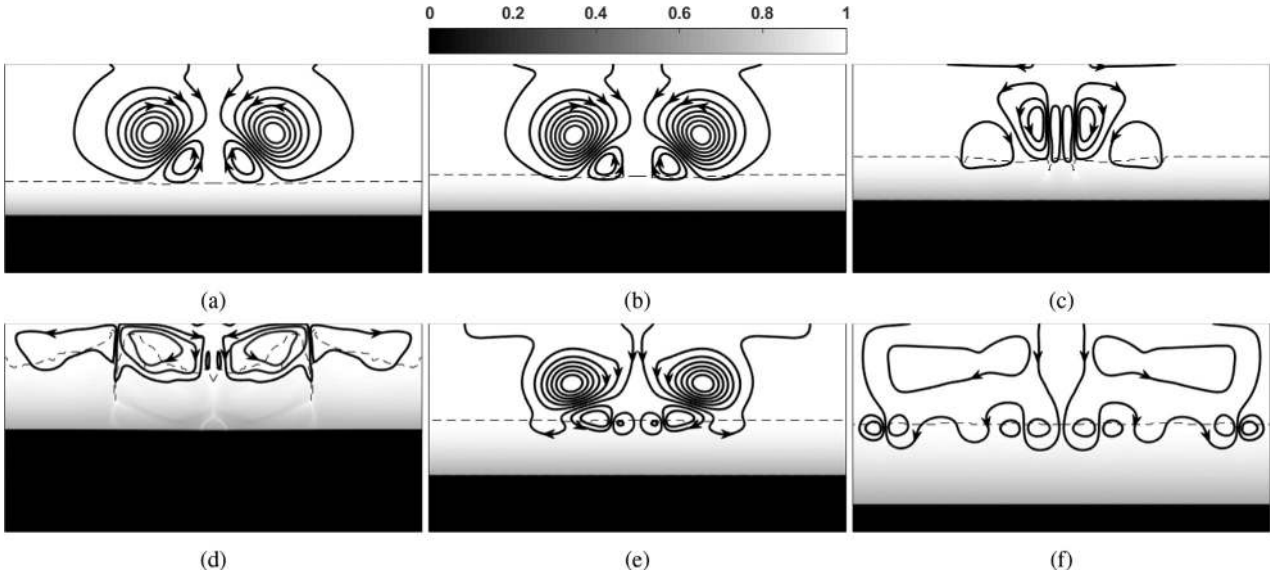

FIG. 14. Numerically predicted liquid fraction and stream function for constant inlet opening size of 40 mm at: (a) $t = 25$ s, $T_c = 523$ K (*b*) $t = 29$ s, $T_c = 523$ K (*c*) $t = 40$ s, $T_c = 523$ K (*d*) $t = 80$ s, $T_c = 523$ K (*e*) $t = 49$ s, $T_c = 623$ K and (*f*) $t = 62$ s, $T_c = 700$ K. Early onset of solutal instability is observed for significantly low cold temperature corresponding to $T_c = 523$ K.

(C_0) through the cavity opening at the top. The thinner mushy region associated with lower cold temperature at the bottom surface allows the incoming melt with a nominal composition (C_0) through the cavity opening to interact and mix with the pure melt at the upper region of the cavity for a substantial duration of the solidification process before the upper bound of the mushy layer is extended till the top surface of the cavity. On the other hand, when a moderate cold temperature is applied at the bottom surface, the upper bound of the mushy layer extends till the top surface at a much earlier stage of the solidification process bounded at the bottom by a slowly growing solid–mushy interface. As a result, the inflow of the melt through the opening at the top surface needs to percolate through the porous mushy region as the pure solid domain slowly extends in the upward direction. The flow resistance of the porous mushy layer does not allow free mixing of incoming melt from the cavity opening with the rest of the liquid distributed in the mushy layer. Owing to the continuous supply of fresh melt with a nominal solute composition (C_0) from the cavity opening, solute-rich liquid phase due to liquid–solid phase transition is flushed out from the mushy region adjacent to the cavity opening and is distributed in the neighboring mushy domain. The combined effect of prolonged shrinkage induced flow through porous mushy region along with a continuous supply of solute lean melt from the cavity opening till the completion of solidification causes severe negative segregation adjacent to this region when moderate cold temperature [Fig. 12(a)] corresponding to 700 K cooling is applied at the bottom surface. However, the severity of this negative segregation perishes drastically for lower values of cold boundary at the bottom surface [Figs. 12(b) and 12(c)]. Ram-head type segregation pattern around the symmetry plane prevails for $T_c = 700$ K and 623 K. However, the size of the ram-head type segregation around the central plane shrinks with decreasing cold boundary temperature. At $T_c = 523$ K, the downward protrusion along the central plane almost vanishes, leaving a small trail of an isolated spot with negative segregation, and the overall effect is a macro-segregation pattern resembling a butterfly around the central plane.

Before concluding the findings from the case study associated with the effect of cold boundary temperature on the freckles formation and macro-segregation under the influence of shrinkage induced flow, we would like to highlight few more interesting observations. The first one among them is concerning the growth rate of the mushy region. It is evident from all the simulation results that the incorporation of shrinkage induced flow enhances the growth rate of the mushy layer. In Fig. 15 evolution of the mushy layer thickness with time is presented for three different cold boundary temperatures. The mushy–liquid and solid–mushy interface locations are monitored until the solutal instability sets in because the mushy–liquid interface has a planer growth till the advent of this event. The time evolution of mushy layer thickness obtained from the simulations involving shrinkage induced flow are compared with those obtained from simulations without considering shrinkage induced flow. As is evident from Fig. 15, for each of the assigned cold boundary temperatures, the mushy layer is predicted to be thicker whenever the effect of shrinkage induces flow is incorporated. The thicker mushy layer perceived by the model involving shrinkage induced flow can be explained as follows. The shrinkage induced flow allows continuous inflow of fresh melt (with nominal composition C_0) to interact and mix with the existing melt inside the cavity. The shrinkage induced flow being conducive to

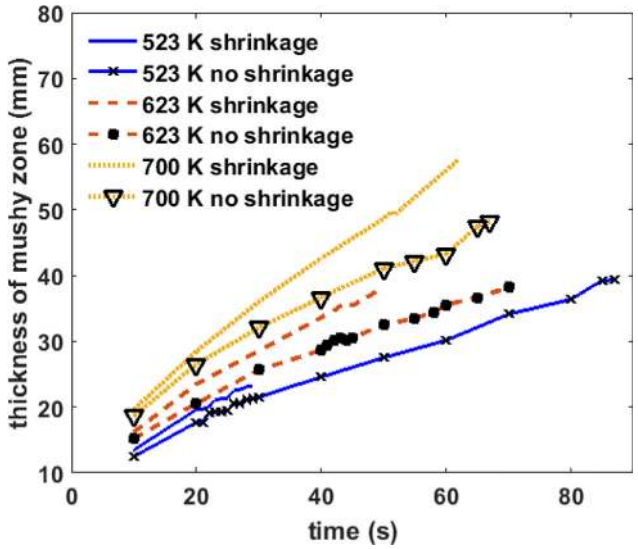

FIG. 15. Comparison of the time evolution of mushy layer thickness in the presence and absence of shrinkage induced flow for varying cold boundary temperature (T_c), before the solutal instability sets in.

better mixing of melt within the cavity causes the dilution of otherwise solute-rich melt adjacent to the mushy–liquid interface. Following the phase diagram (Fig. 3), dilution of solute concentration is coherent with the rise in local liquidus temperature. Thus, the increase in local liquidus temperature caused by the dilution of solute concentration adjacent to the mushy–liquid interface promotes faster growth of the mushy region when shrinkage induced flow is taken into account. On the other hand, in the absence of shrinkage induced flow, the pure melt region remains quiescent until the onset of solutal instability. Owing to the negligibly small solutal diffusivity $\mathcal{O}(\sim 10^{-9}\mathrm{m}^2/\mathrm{s})$ and absence of convective mixing mechanism prior to the onset of solutal instability, a solute-rich melt layer builds up adjacent to the mushy–liquid interface. The solute-rich melt adjacent to the mushy–liquid interface having a lower liquidus temperature hinders the growth rate of the mushy layer. One more important observation from Fig. 15 is associated with the onset timing of solutal instability. For all the assigned cold boundary temperatures (700K, 623 K, and 523 K) in Fig. 15, we find that onset of solutal instability sets in at an earlier time instant whenever shrinkage induced flow is accounted for. As has been mentioned earlier, this early onset of solutal instability can be attributed to the perturbation of the metastable solutal buoyancy field adjacent to the mushy–liquid interface by the shrinkage induced flow combined with a faster growth rate of the mushy–liquid interface.

Next, the onset timings of solutal instability and the mushy–liquid interface locations associated with this onset for a range of cold boundary temperature are compared for simulation results involving the presence and absence of shrinkage induced flow. Figure 16(a) shows that for the entire range of cold boundary temperature under consideration, the shrinkage induced flow causes early onset of solutal instability. The lower the cold boundary temperature earlier is the onset of solutal instability compared to no-shrinkage induced flow assumption. In terms of the mushy–liquid interface location, the solutal instability sets in at a comparatively lower height of the interface

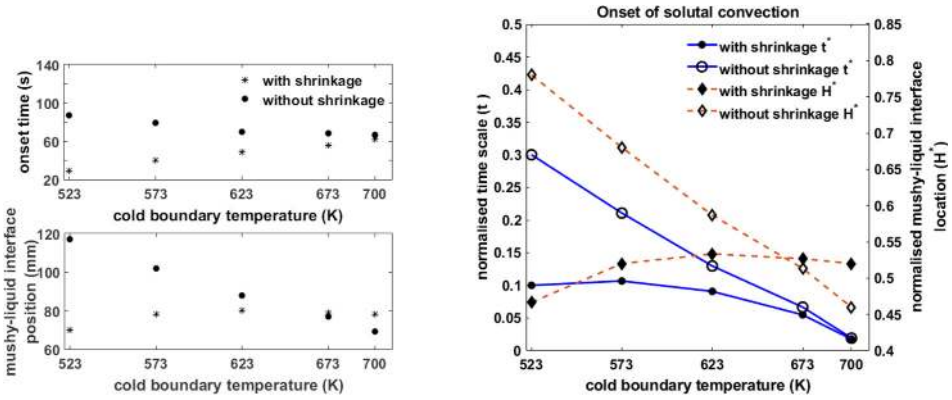

FIG. 16. Comparison of the onset time and associated height of mushy–liquid interface of solutal instability in the presence and absence of shrinkage induced flow for varying cold boundary temperature (T_c). (a) Dimensional representation of onset time and mushy–liquid interface height and (b) normalized representation of onset time and mushy–liquid interface height.

for no-shrinkage induced flow assumption when cooling at the cold boundary is moderate (corresponding to $T_c = 700$ K and 673 K). However, with lower and lower cold temperature ($T_c = 623$ K, 573 K, and 523 K) a reverse trend sets in. Lower cold temperature intensifies the shrinkage induced inflow of melt into the cavity. Lower the cold temperature, deeper is the penetration of the shrinkage induced inflow into the melt region. As a result, perturbation of the metastable solutal buoyancy field adjacent to the mushy–liquid interface by the shrinkage induced incoming flow occurs at progressively lower heights of mushy–liquid interface location with lowering the cold temperature. Since the timescale to attain complete solidification in the cavity and interface growth rates is directly connected with the cold boundary temperatures at the bottom surface, representation of the onset of the solutal instability with respect to a normalized timescale and a normalized mushy–liquid interface location is much more desirable. In Fig. 16(b), the onset of the solutal instability is presented with respect to the normalized timescale and normalized mushy–liquid interface location for five different cold boundary temperatures. The normalized timescale (t^*) is obtained by dividing the dimensional time with the total time required to attain the complete solidification in the cavity ($t^* = t/\Delta t_{tot}$). Similarly the normalized mushy–liquid interface location (H^*) is defined as the ratio of mushy–liquid interface height ($H_{i(m-l)}$) to the cavity height (H_C), and is given by $H^* = H_{i(m-l)}/H_C$. For all the assigned values of cold boundary temperature, simulations pertaining to shrinkage induced flow are found to promote early onset of plume formation as compared to those in the absence of shrinkage induced flow when the onset is plotted against normalized timescale. With increasing degree of cooling at the bottom surface ($T_c = 623$ K, 573 K, and 523 K) the normalized onset timing involving shrinkage induced flow is fairly insensitive to the cold boundary temperature, i.e., dt^*_{onset}/dT_c is very small. However, in the absence of shrinkage induced flow, the normalized onset timing is highly sensitive to the cold boundary temperature for the entire range T_c with large t^*_{onset} *Vs.* T_c slope. As is evident from Fig. 16(b), t^*_{onset} increases monotonically with lowering the cold temperature T_c in the absence of shrinkage induced flow, while t^*_{onset} associated with shrinkage induced flow manifests an asymptotic behavior for the same indicating early onset of plume formation. Therefore, we can conclude that the shrinkage induced flow expedite the onset of solutal instability substantially for low cold boundary temperature at the bottom surface. Next, we verify the onset of plume formation with respect to the normalized mushy–-liquid interface location [Fig. 16(b)]. For moderate values of cold temperatures at the bottom surface ($T_c = 700$ K and 673 K), the height of normalized mushy–liquid interface corresponding to the onset of plume formation (H^*_{onset}) is found to be lower when shrinkage induced flow is not considered. The reason behind this outcome can be attributed to the faster growth rate of the mushy layer associated with shrinkage induced flow. For instance, the difference between the normalized onset time instant corresponding to $T_c = 700$ K is smallest for case studies associated with and without the consideration of shrinkage induced flow, but the normalized mushy–liquid interface height (H^*_{onset}) corresponding to shrinkage induced flow consideration is found to surpass the one obtained without shrinkage induced flow. As we keep lowering the cold boundary T_c, the same trend prevails till some range of T_c ($T_c = 673$ K). With lowering T_c values, the onset time lag between these two cases (without and with shrinkage induced flow) becomes more and more evident. However, the gap between the onset locations in terms of normalized mushy–liquid interface heights diminishes, leading to a crossover point below $T_c = 673$ K. After this crossover point, solutal instability stimulated by shrinkage induced flow sets in at progressively lower heights of normalized mushy–liquid interface locations (H^*_{onset}) as T_c is decreased further and further. This trend is completely contrary to the ever-increasing H^*_{onset} behavior with progressively smaller values of T_c in the absence of shrinkage induced flow.

The results concerning the early onset of solutal instability (Fig. 16) associated with low cold temperature compelled us to revisit the effect of opening size on the onset phenomena once more. During the previous study considering cold boundary temperature to be at 700 K, we found the effect of opening size on the onset time and location to be negligible. Since smaller opening size enhances the strength of shrinkage induce flow, a similar outcome described by Fig. 16 should have been observed. Therefore, the insensitivity of the onset of solutal instability with respect to the inlet opening size at $T_c = 700$ K should be justified. The intensity of shrinkage induce flow is directly dependent on the growth rate of the pure solid front, and the growth rate of the pure solid front has a direct correspondence with the extent of cooling at the bottom surface. At $T_c = 700$ K the growth rate of pure solid front is significantly smaller than that obtained for $T_c = 523$ K. Therefore, the intensity of shrinkage induce flow is expected to be

much larger for $T_c = 523$ K than for $T_c = 700$ K. Also, the effect of inlet opening size on the onset of solutal instability should be much more prominent when $T_c = 523$ K. Figure 17 shows the effect of varying inlet opening size on the onset of solutal instability for $T_c = 523$ K and $T_c = 700$ K. And indeed, we find the onset of solutal instability to be significantly sensitive to the inlet opening size $T_c = 523$ K (Fig. 17); particularly when the opening size varies from 40 mm to 6 mm. However, we encounter a very strange feature of the onset profile on the normalized time and mushy–liquid interface length scale for $T_c = 523$ K, when the inlet opening size is reduced from 20 mm to 6 mm. As we keep on decreasing the opening size till 20 mm, t^* and H^* corresponding to the onset of solutal instability reduce monotonically signifying early onset phenomena. But the reduction of the opening size below 20 mm upsets this monotonic trend drastically, featuring onset delay with higher values of t^* and H^*. Thus, it is necessary to justify the cause of this onset delay as the inlet opening size is reduced below 20 mm.

As mentioned earlier, the onset sites for plume formation are closely associated with the regions along with the mushy–liquid interface, where the accumulation of high solute concentration sets in representing the metastable concentration field (Fig. 13). Weaker shrinkage induced flow associated with moderate cold temperature at the bottom surface and larger inlet opening size does not penetrate the mushy region and gets dissipated solely within the pure melt region. However, the slight perturbation of the metastable solutal field adjacent to the mushy–liquid interface caused by this weak shrinkage induced flow gives rise to the early onset of plume formation. Progressive early onsets of plume formation predicted in Fig. 17 for 40–20 mm inlet opening sizes can be attributed to the restriction of the shrinkage induced flow within the pure melt region only. On the other hand, large cooling combined with smaller inlet opening size allows the shrinkage induced flow to grow strong enough to penetrate the mushy region itself [Figs. 18(a) and 18(b)]. As a result, the upward movement of the solute-rich melt within the mushy region adjacent to

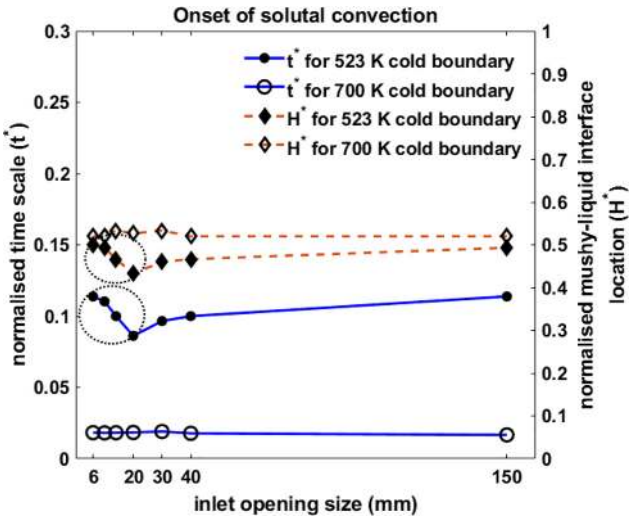

FIG. 17. Normalized representation of onset times and associated mushy–liquid interface heights of solutal instability for varying inlet opening size, namely 6 mm, 10 mm, 14 mm, 20 mm, 30 mm, 40 mm, and 150 mm, for $T_c = 523$ K and 700 K.

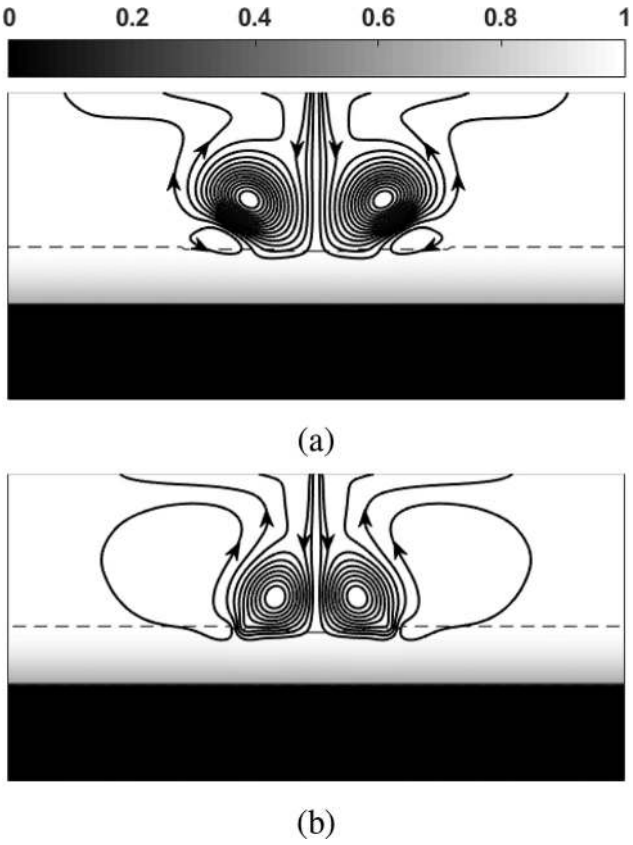

FIG. 18. Numerically predicted liquid fraction and stream function at the onset of solutal instability: (a) $t_{onset} = 32$ s for 10 mm inlet opening size and (b) $t_{onset} = 33$ s for 6 mm inlet opening size.

the symmetry plane of the cavity is not only hindered by the incoming shrinkage induced flow, but this naturally occurring solute-rich melt is also pushed back into the mushy region leading to the redistribution of solute-rich melt within the mushy region. The redistribution of solute-rich melt within the mushy region eventually culminates to plume formation sites where the primary convection cells due to shrinkage induced flow creates a suction effect owing to the net upward movement of the melt adjacent to the mushy–liquid interface. The suppression and redistribution of the naturally occurring solute distribution within the mushy region by the high intensity shrinkage induced flow result in an overall delay of the onset of plume formation. With smaller and smaller inlet opening sizes below 20 mm, the onset occurs at a more and more delayed time interval (Fig. 17). However, this nonintuitive effect of the inlet opening size on the onset of solutal instability is prominent only when the cavity is subjected to very low cold temperature at the bottom surface.

It is pertinent to mention here that barring few case studies involving very low intensity shrinkage induced flow associated with higher values of cold boundary temperature T_c and large inlet opening size, shrinkage induced flow always promotes early onset of solutal instability with respect to the baseline case without involving shrinkage induced flow. The early or late onset of solutal instability discussed in

this work is in the context of variation in shrinkage induced flow intensity from lower to higher value. In fact, when the cold boundary temperature (T_c) is very low, baseline case without involving shrinkage induced flow does not even manifest channel formation. However, incorporation of the shrinkage induced flow with the same cold temperature boundary condition leads to freckle formation in solidification domain. In support of this statement, liquid fraction and stream function at the onset of solutal instability (Fig. 19) and a comparison between macro-segregation pattern obtained after completion of solidification process with and without shrinkage induced flow effect are presented in Fig. 20. The case study involves solidification of Al-30 wt. % Mg alloy in the cavity with inlet opening size 10 mm opening size and $T_c = 300$ K. Shrinkage induced flow is found to assist instability to grow inside the mushy layer, leading to channel formation Fig. 20(a). However, in the absence of shrinkage induced flow, although there exist some macro-segregation profiles adjacent to the top surface, it is definitely not a pattern akin to the distinctive channel formation Fig. 20(b). Therefore, we conclude that shrinkage induced flow promotes the onset of solutal instability to grow enhancing the freckling phenomena.

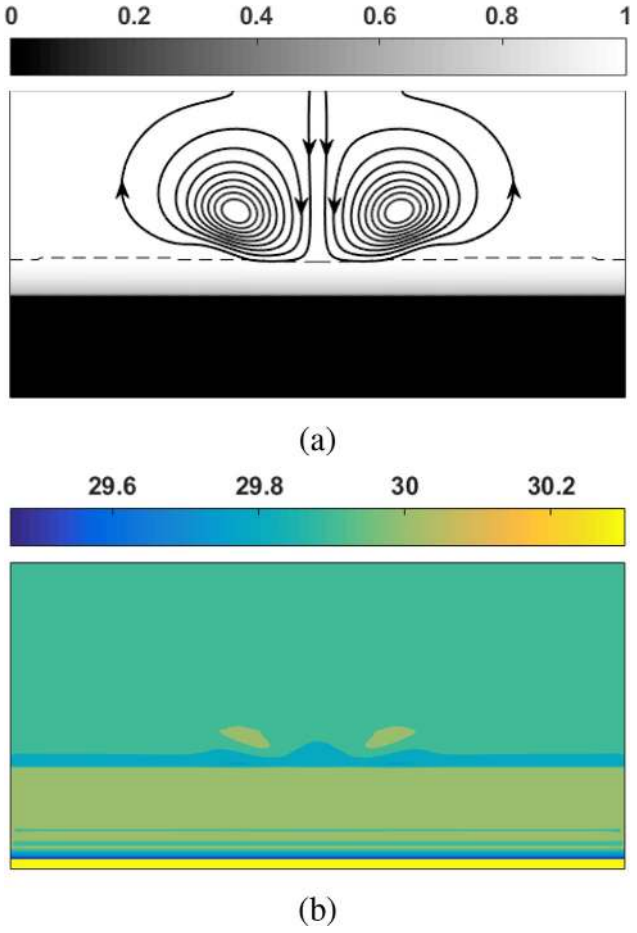

FIG. 19. (a) Numerically predicted liquid fraction and stream function at the onset of solutal instability and (b) corresponding solute concentration distribution at $t_{onset} = 19$ s for 10 mm inlet opening size and 300 K cold boundary temperature.

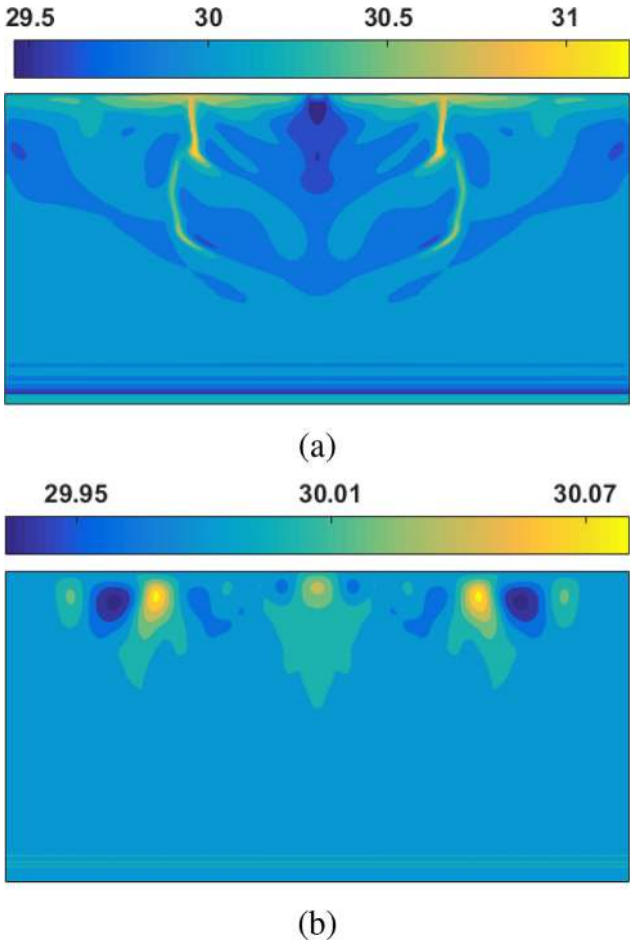

FIG. 20. Solute distribution after complete solidification for the case with (a) shrinkage and (b) no-shrinkage assumption for 10 mm inlet opening size and 300 K cold boundary temperature.

4. Scaling analysis

In this subsection, a scaling analysis is attempted in order to obtain a generalized understanding of the influence of shrinkage induced flow on the onset of solutal instability. The first attempt to obtain a meaningful scaling analysis involves nondimensionalization of governing equations by choosing physically relevant length scale, timescale, reference velocity, pressure, temperature and solute composition scales associated with the problem definition. These reference scales are reported by Worster *et al.*, and Sajja and Felicelli.[5,40,63] The reference length scale L_{ref} is considered to be of the order of primary dendrite arm spacing ($\sim 10^{-4} m$),[40,63] $u_{ref} = \sqrt{g\beta_C C_0 L_{ref}}$,[63] reference timescale $t_{ref} = L_{ref}/u_{ref}$,[40,63] $\rho_{ref} = \rho_l$, and $p_{ref} = \rho_l u_{ref}^2$.[5,40,63] Nondimensional temperature and solute concentrations are defined as:[5] $\theta = (T - T_L(C_0))/(T_L(C_0) - T_e) = (T - T_L(C_0))/\Delta T$ and $\bar{C} = (C - C_0)/(C_0 - C_e) = (C - C_0)/\Delta C$. Defining other nondimensional parameters as: $X = x/L_{ref}$, $Y = y/L_{ref}$, $\tau = t/t_{ref}$, $\bar{u} = u/u_{ref}$, $\bar{v} = v/u_{ref}$, $\bar{\rho} = \rho/\rho_{ref}$ and $\bar{p} = p/p_{ref}$ we obtain the following set of nondimensional governing equations:

Continuity

$$\nabla.(\bar{\rho}\bar{\mathbf{V}}) = \beta\frac{\partial g_l}{\partial \tau}, \tag{11}$$

Momentum

$$\frac{\partial}{\partial\tau}(\bar{\rho}\bar{u}) + \nabla.(\bar{\rho}\bar{\mathbf{V}}\bar{u}) = \frac{1}{Re}\nabla^2(\bar{\rho}\bar{u}) - \frac{\partial\bar{p}}{\partial X} - \frac{1}{ReDa}\frac{g_s^2}{g_l^3}(\bar{\rho}\bar{u}) - \nabla.\left(\frac{\rho_s}{\rho_l}\frac{g_s}{g_l}\bar{\rho}\bar{\mathbf{V}}\bar{u}\right), \tag{12}$$

$$\frac{\partial}{\partial\tau}(\bar{\rho}\bar{v}) + \nabla.(\bar{\rho}\bar{\mathbf{V}}\bar{v}) = \frac{1}{Re}\nabla^2(\bar{\rho}\bar{v}) - \frac{\partial\bar{p}}{\partial Y} - \frac{1}{ReDa}\frac{g_s^2}{g_l^3}(\bar{\rho}\bar{v}) - \nabla.\left(\frac{\rho_s}{\rho_l}\frac{g_s}{g_l}\bar{\rho}\bar{\mathbf{V}}\bar{v}\right) + \frac{Gr_T}{Re^2}(\theta+1) + \frac{Gr_C}{Re^2}(\overline{C_l}+1), \tag{13}$$

Energy

$$\frac{\partial}{\partial\tau}(\bar{\rho}\theta) + \nabla.(\bar{\rho}\bar{\mathbf{V}}\theta) = \frac{1}{Re}\left(\nabla.\left(\frac{1}{Pr}\nabla\theta\right)\right) - a'\nabla.(\bar{\rho}\bar{\mathbf{V}}\theta) - a'\frac{T_L(C_0)}{\Delta T}\nabla.(\bar{\rho}\bar{\mathbf{V}}) - \frac{\rho_s}{\rho_l}\frac{1}{Ste}\frac{\partial}{\partial\tau}(g_l) - a'\frac{\partial}{\partial\tau}(\theta g_l) - a'b'\frac{T_L(C_0)}{\Delta T}\frac{\partial}{\partial\tau}(g_l), \tag{14}$$

where

$$a' = \left(\frac{c_{pl}}{c_{ps}} - 1\right); \quad b' = 1 - \frac{\rho_s T_e}{\rho_l T_L(C_0)}.$$

Species

$$\frac{\partial}{\partial\tau}(\bar{\rho}\bar{C}) + \nabla.(\bar{\rho}\bar{\mathbf{V}}\bar{C}) = \frac{1}{ReSc}\nabla.(g_l\nabla\bar{C}) + \frac{1}{ReSc}\nabla.(g_l\nabla(\overline{C_l}-\bar{C})) - \nabla.(\bar{\rho}\bar{\mathbf{V}}(\overline{C_l}-\bar{C})). \tag{15}$$

Nondimensional parameters like contraction ratio (β), Reynolds number (Re), Darcy number (Ds), thermal and solutal Grashof numbers (Gr_T and Gr_C), Prandtl nummber (Pr), Stefan number (Ste), and Schmidt number (Sc) appearing in Eqs. (11)–(15) are defined as follows:

$$\beta = \frac{\rho_s - \rho_l}{\rho_l}; \quad Re = \frac{u_{ref}L_{ref}}{\nu}; \quad Da = \frac{K_0}{L_{ref}^2};$$

$$Gr_T = \frac{g_a\beta_T(T_L(C_0)-T_e){L_{ref}}^3}{\nu^2}; \quad Gr_C = \frac{g_a\beta_C(C_0-C_e){L_{ref}}^3}{\nu^2};$$

$$Pr = \frac{\nu}{k/(\rho_l c_{ps})}; \quad Ste = \frac{\Delta T c_{ps}}{h_{sl}}; \quad Sc = \frac{\nu}{D_l}$$

The nondimensional representation of conservation equations [Eqs. (11)–(15)] has provided meaningful nondimensional parameters like contraction ratio (β), Reynolds number (Re), Darcy number (Ds), thermal and solutal Grashof numbers (Gr_T and Gr_C), Prandtl number (Pr), Stefan number (Ste), and Schmidt number (Sc) along with many other nondimensional groups (like a', b', $T_L(C_0)/\Delta T$, etc.) relevant to the alloy solidification process. However, none of these parameters helps us to characterize the onset of solutal instability with respect to the inlet opening size, cavity height and cooling condition at the bottom boundary. In fact the reference length scale and nondimensional scheme for temperature do not allow us to consider the effects of the cavity aspect ratio (H_C/W_C), the inlet opening size, and cooling condition at the bottom wall. While the cavity aspect ratio decides the penetration depth of the shrinkage induced flow, the ratio inlet opening size with cavity width along with cold boundary temperature (T_c) defines the magnitude of the same. Therefore, all these three aspects should be reflected in a scaling analysis to analyze the solutal instability phenomena in the presence of shrinkage induced flow and a different approach must be considered other than the one obtained through nondimensionalization of conservation equations [Eqs. (11)–(15)].

The alternative scaling analysis provided here, albeit an ad hock one in nature, is found to be much more effective in terms of predicting the dependence of solutal instability on shrinkage induced flow. In this approach, we are concerned about two different velocity scales, namely (i) a reference velocity scale corresponding to shrinkage induced flow (u_{ref}^{sh}) and (ii) a reference velocity scale corresponding solutal buoyancy driven flow (u_{ref}^{sb}. Estimation of u_{ref}^{sb} is similar to the one presented in the previous scaling approach, and is given by $u_{ref}^{sb} = \sqrt{g\beta_C C_0 L_{ref}}$. However, estimation of u_{ref}^{sh} is not so straightforward. To obtain u_{ref}^{sh} a semi-infinite solidification model described by Dantzig and Rappaz[8] is used. This particular semi-infinite model defines the solid–liquid interface growth rate during the solidification of a pure substance as follows:[8]

$$u_i^* = \phi\sqrt{\frac{\alpha_s}{t}}. \tag{16}$$

The estimation of constant nondimensional parameter ϕ in Eq. (16) involves the knowledge of phase thermal diffusivities, cold boundary temperature (T_c), initial temperature (T_i), freezing temperature (T_m), and latent heat; and the transcendental equation to estimate ϕ contains all these parameters arranged in nondimensional groups as follows:[8]

$$\frac{\rho_s h_{sl}\alpha_s\sqrt{\pi}}{k_s(T_m-T_c)} - \frac{\exp(-\phi^2)}{\phi erf(\phi)} + \sqrt{\frac{\alpha_s}{\alpha_l}}\frac{k_l}{k_s}\left(\frac{T_i-T_m}{T_m-T_c}\right) \times \frac{\exp(-\phi^2\alpha_s/\alpha_l)}{\phi erfc\left(\phi\sqrt{\alpha_s/\alpha_l}\right)} = 0. \tag{17}$$

As we are dealing with alloy solidification here involving the presence of mushy layer of finite thickness between the pure solid and liquid phases, the interface between the pure solid and mushy phase is at temperature T_e. Therefore, we replace freezing point T_m with T_e in Eq. (17) and estimate ϕ for given T_c and T_i. Once ϕ is calculated, considering order of magnitude for time to be unity in Eq. (16), we obtain a tentative scaling for growth rate of pure solid front given by; $u_i^* = \phi\sqrt{\alpha_s}$. At the very beginning of the solidification process, this semi-infinite domain consideration is aptly valid. The estimation of reference scale for solid interface growth rate (u_i^*) leads to the estimation of u_{ref}^{sh} from the conservation of mass principle in the following manner.

$$\rho_l W_{in} u_{ref}^{sh} \approx (\rho_s - \rho_l) W_C u_i^*. \tag{18}$$

Equation (18) provides us with a suitable scaling for shrinkage induced flow given by $u_{ref}^{sh} = (\rho_s - \rho_l)W_C u_i^*/(\rho_l W_{in})$. The ratio of

Reynolds number corresponding to incoming shrinkage flow ($Re_{SIF} = u_{ref}^{sh} L_{ref}/\nu$) and solutal Grashof number ($Gr_C = (g_a \beta_C (C_0 - C_e) L_{ref}^3)/\nu^2$ provides us with the information regarding the relative strength of these two different flow mechanisms. However, the effect of cavity aspect ratio ($AR = H_C/W_C$) still needs to be addressed. A larger value of AR indicates dissipation of shrinkage induced flow in the melt domain much above the growing mushy–liquid interface, the domain associated with the origination of solutal instability. Therefore, higher value of AR will attenuate the effect of shrinkage induced flow on solutal instability. Combining all these physical constraints, we propose a nondimensional group given by $Re_{SIF}/(Gr_C.AR)$ in order to classify onset behavior of solutal instability. Using this newly defined scaling parameter on case studies discussed in Sec. V B, we find that $Re_{SIF}/(Gr_C.AR) \leq 0.9$ corresponds to no effect of shrinkage induce flow on the onset of solutal instability, i.e., inclusion of shrinkage induced flow does not have any effect on the onset time of the solutal instability with respect to the baseline case without involving shrinkage induced flow. Condition $Re_{SIF}/(Gr_C.AR) \geq 0.9$ always corresponds to the early onset of solutal instability with respect to the baseline case involving freckle formation in the absence of shrinkage. For the range $0.9 \leq Re_{SIF}/(Gr_C.AR) \leq 2.0$, larger the value of $Re_{SIF}/(Gr_C.AR)$ earlier is the onset of solutal instability Figs. 21(a) and 21(b). However, for $Re_{SIF}/(Gr_C.AR) > 2.0$ this trend is reversed, i.e., larger the value of $Re_{SIF}/(Gr_C.AR)$ more delayed is the onset of solutal instability Figs. 21(a) and 21(b).

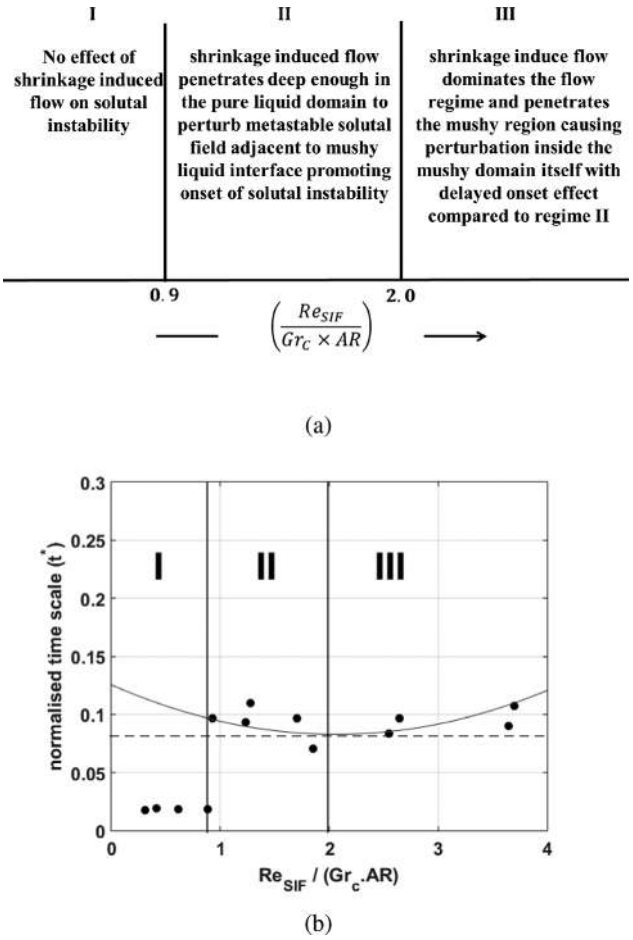

FIG. 21. Criterion describing the onset of solutal instability.

VI. CONCLUSIONS

A numerical model is proposed that predicts the effect of the shrinkage induced flow on freckling phenomena during directional solidification of binary alloy. The cooling condition and geometrical parameters define the intensity of shrinkage induced flow. The shrinkage induced flow is found to play a key role in perturbing the metastable melt solutal field develop inside and adjacent to the mushy layer during solidification of alloys involving lighter solute rejection in the melt. The mutual interaction between shrinkage induced flow and solutal instability leads to a complex flow patterns within the mushy and liquid domains. The most important outcomes inferred from this study are as follows:

1. A binary alloy solidification model is proposed addressing the influence of shrinkage induced flow by implementing suitable volume fraction updating scheme. The proposed model is used to analyze the effect of shrinkage induced flow on freckle formation considering directional solidification of binary alloy (Al-30 wt.% Mg) in a bottom cooled cavity.
2. The effect of grid resolution and time step resolution on the simulation results is carried out for solidification process involving freckle formation in presence of shrinkage induced flow. Al-30 wt.% Mg is considered to the model binary system. It is inferred that the phenomena is highly unstable and achieving complete grid resolution and time step independence is not possible.
3. Model validation is performed with respect to a benchmark problem involving inverse segregation obtained for the bottom-up solidification of Al-4.1 wt.% Cu alloy in the presence of shrinkage induced flow and characterized by heavier solute rejection in the melt during liquid–solid phase transition. Simulation result from the proposed model is compared with existing numerical and experimental data reported in literature furnishing reasonably good agreement.
4. General attributes of shrinkage induced flow on freckle formation is studied for a very high value of cold boundary temperature ($T_c = 720$ K) while keeping inlet opening size to be 40 *mm*. The results inferred that the convection field in the melt region at the initial stage of the solidification process is governed solely by the shrinkage induced flow, followed by the advent of the solutal instability adjacent to mushy–liquid interface leading to complex flow interactions. One of the major influences of the shrinkage induced flow is manifested by the lateral bending of plumes away from the central plane of symmetry leading to the formation of oblique channels.
5. Case study involving the effect of varying inlet opening size is analyzed for $T_c = 700$ K. It is inferred from the study that the opening size has a substantial impact on the severity of the solute lean region near the opening. The severity of negative segregation adjacent to the opening at the cavity top surface varies from severe to mild entrapment of solute lean composition for small to full opening.

6. Next, the effect of cold temperature on the onset of instability and macro-segregation is investigated. A shift of cooling temperature at the bottom surface from high to moderately low range causes the onset of the solutal instability to occur at a comparatively greater height of the mushy–liquid interface. However, further reduction of bottom surface temperature intensifies the strength of shrinkage induced flow, allowing it to perturb the meta-stable solutal field adjacent to the mushy–liquid interface at an early stage of solidification, leading to an early onset of solutal instability. Low cooling temperature also negates the severity of the negative segregation. However, for the entire range of cooling, the thickness of the mushy layer is always found to be greater in the presence of shrinkage induced flow as compared to the predicted mushy layer thickness obtained under the no-shrinkage assumption. The thicker mushy region obtained under the influence of shrinkage induced flow is attributed to the entrainment of fresh melt with nominal composition into the upper bound of the mushy layer, leading to an overall elevation of local liquidus temperature in that region.
7. In order to investigate the effect of cooling on the onset of solutal instability, a case study is carried out by varying the cold boundary temperature, while considering the central opening sized at the upper surface of the cavity to be 40 mm. In terms of onset timing, the results involving shrinkage induced flow consistently predicted early onset of solutal instability as compared to those obtained with no shrinkage assumption. With low cooling temperatures, the onset time difference became substantially large between the studies associated with shrinkage and no-shrinkage assumptions. In terms of the height of the mushy–liquid interface, for high and moderate cold temperatures, solutal instability is found to be triggered at a lower position of this interface in the absence of shrinkage induced flow. However, the gap between the onset locations with and without shrinkage induced flow assumptions in terms of mushy–liquid interface heights diminishes as the cold boundary temperature is lowered, leading to a crossover point below a certain range of T_c. Further lowering of the cold boundary temperature consistently reduces the mushy–liquid interface height corresponding to the onset of solutal instability for shrinkage induced flow assumption, which is a complete contrary to the ever-increasing behavior of the same under the no-shrinkage assumption.
8. The effect of shrinkage induced flow on the onset of solutal instability being more prominent for large cooling, the influence of cavity inlet opening size is revisited considering T_c at 523 K while varying the opening size from 40–6 mm. Over the range of opening size 40–20 mm, both time interval and mushy–liquid interface height corresponding to the onset of solutal instability manifested a monotonically decreasing trend signifying the early onset of solutal instability. The early onset of plume formation for this range of inlet opening size (40–20 mm) is attributed to the perturbation of the meta-stable solutal buoyancy field by the shrinkage induced flow within the pure melt region only. However, lowering the opening size below 20 mm intensifies the shrinkage induced flow significantly and allows it to penetrate the mushy region itself, leading to the suppression and redistribution of naturally occurring solutal instability of the liquid phase within the mushy layer. The redistribution of the solute-rich melt inside the mushy layer eventually leads to plume formation sites along the path of least resistance where primary circulations corresponding to shrinkage induced flow lifts off the fluid from the mushy–liquid interface to the pure melt domain. The entire process of suppression and redistribution of the solutal instability within the mushy region leads to an overall delay of the onset of plume formation, and this effect is evident only when the solidification process is simultaneously subjected to large cooling and small inlet opening size.
9. A scaling analysis is attempted to have a criterion that assess the relative magnitude of shrinkage convection and solutal buoyancy driven natural convection. A nondimensional group in the form $Re_{SIF}/(Gr_C.AR)$ is proposed. It was inferred that $Re_{SIF}/(Gr_C.AR) \leq 0.9$ corresponds to no effect of shrinkage induce flow on the onset of solutal instability. Condition $Re_{SIF}/(Gr_C.AR) \geq 0.9$ always corresponds to the early onset of solutal instability with respect to the baseline case involving freckle formation in the absence of shrinkage. For the range $0.9 \leq Re_{SIF}/(Gr_C.AR) \leq 2.0$, larger the value of $Re_{SIF}/(Gr_C.AR)$ earlier the onset of solutal instability. However, for $Re_{SIF}/(Gr_C.AR) > 2.0$ this trend is reversed, i.e., larger the value of $Re_{SIF}/(Gr_C.AR)$ later the onset of solutal instability

ACKNOWLEDGMENTS

The authors appreciate the immense support received from the Department of Science and Technology (DST), India (Grant No. DST/TMD/MES/2K17/44), and IIT Jodhpur Seed Grant (Grant No. I/SEED/PRC/20150023). The authors are also grateful to acknowledge the work performed by Grammarly Application while preparing the manuscript.

DATA AVAILABILITY

The data that support the findings of this study are available from the corresponding author upon reasonable request.

REFERENCES

[1]M. Flemings, *Solidification Processing* (Mcgraw-Hill, New York, 1974).
[2]K. Fisher, "The effects of fluid flow on the solidification of industrial castings and ingots," PhysicoChem. Hydrodyn. **2**, 311–326 (1981).
[3]M. G. Worster, "Solidification of an alloy from a cooled boundary," J. Fluid Mech. **167**, 481–501 (1986).
[4]M. G. Worster, "Natural convection in a mushy layer," J. Fluid Mech. **224**, 335–359 (1991).
[5]M. G. Worster, "Instabilities of the liquid and mushy regions during solidification of alloys," J. Fluid Mech. **237**, 649–669 (1992).
[6]M. G. Worster and R. C. Kerr, "The transient behaviour of alloys solidified from below prior to the formation of chimneys," J. Fluid Mech. **269**, 23–44 (1994).
[7]D. M. Stefanescu, *Science and Engineering of Casting Solidification* (Springer, 2015).
[8]J. A. Dantzig and M. Rappaz, *Solidification:-Revised & Expanded* (EPFL Press, 2016).
[9]X. Zhang, L-l Wang, H. Zhu, and C. Zeng, "Modeling of salt finger convection through a fluid-saturated porous interface: Representative elementary volume scale simulation and effect of initial buoyancy ratio," Phys. Fluids **32**, 082109 (2020).
[10]J.-H. Xie, K. Julien, and E. Knobloch, "Fixed-flux salt-finger convection in the small diffusivity ratio limit," Phys. Fluids **32**, 126601 (2020).

[11]J. Sarazin and A. Hellawell, "Channel formation in Pb-Sn, Pb-Sb, and Pb-Sn-Sb alloy ingots and comparison with the system NH_4 Cl-H_2O," Metall. Trans. A **19**, 1861–1871 (1988).
[12]S. D. Felicelli, J. Heinrich, and D. R. Poirier, "Simulation of freckles during vertical solidification of binary alloys," Metall. Mater. Trans. B **22**, 847–859 (1991).
[13]H. Jamgotchian, H. N. Thi, N. Bergeon, and B. Billia, "Double-diffusive convective modes and induced microstructure localisation during solidification of binary alloys," Int. J. Thermal Sci. **43**, 769–777 (2004).
[14]Q. Diao and H.-L. Tsai, "Modeling of solute redistribution in the mushy zone during solidification of aluminum-copper alloys," Metall. Trans. A **24**, 963–973 (1993).
[15]J. Chen and H.-L. Tsai, "Inverse segregation for a unidirectional solidification of aluminum-copper alloys," Int. J. Heat Mass Transfer **36**, 3069–3075 (1993).
[16]Z. Gao, W. Jie, Y. Liu, and H. Luo, "Solidification modelling for coupling prediction of porosity and segregation," Acta Mater. **127**, 277–286 (2017).
[17]Z. Gao, W. Jie, Y. Liu, Y. Zheng, and H. Luo, "A model for coupling prediction of inverse segregation and porosity for up-vertical unidirectional solidification of Al–Cu alloys," J. Alloys Compd. **797**, 514–522 (2019).
[18]M. I. Bergman, D. R. Fearn, J. Bloxham, and M. C. Shannon, "Convection and channel formation in solidifying Pb-Sn alloys," Metall. Mater. Trans. A **28**, 859–866 (1997).
[19]C. Chen and F. Chen, "Experimental study of directional solidification of aqueous ammonium chloride solution," J. Fluid Mech. **227**, 567–586 (1991).
[20]P. Emms and A. Fowler, "Compositional convection in the solidification of binary alloys," J. Fluid Mech. **262**, 111–139 (1994).
[21]F. Chen, J. W. Lu, and T. L. Yang, "Convective instability in ammonium chloride solution directionally solidified from below," J. Fluid Mech. **276**, 163–187 (1994).
[22]C. Chen, "Experimental study of convection in a mushy layer during directional solidification," J. Fluid Mech. **293**, 81–98 (1995).
[23]V. Kumar, A. Srivastava, and S. Karagadde, "Generalized regimes for the formation of stratified regions during freezing of multi-component mixtures," Phys. Fluids **31**, 123602 (2019).
[24]A. Chiareli, H. E. Huppert, and M. G. Worster, "Segregation and flow during the solidification of alloys," J. Crystal Growth **139**, 134–146 (1994).
[25]A. Chiareli and M. G. Worster, "Flow focusing instability in a solidifying mushy layer," J. Fluid Mech. **297**, 293–305 (1995).
[26]T. Schulze and M. G. Worster, "A numerical investigation of steady convection in mushy layers during the directional solidification of binary alloys," J. Fluid Mech. **356**, 199–220 (1998).
[27]C. Chung and M. G. Worster, "Steady-state chimneys in a mushy layer," J. Fluid Mech. **455**, 387 (2002).
[28]R. F. Katz and M. G. Worster, "Simulation of directional solidification, thermochemical convection, and chimney formation in a Hele-Shaw cell," J. Comput. Phys. **227**, 9823–9840 (2008).
[29]S. Peppin, H. E. Huppert, and M. G. Worster, "Steady-state solidification of aqueous ammonium chloride," J. Fluid Mech. **599**, 465 (2008).
[30]P. R. Chakraborty and P. Dutta, "Study of freckles formation during directional solidification under the influence of single-phase and multiphase convection," J. Therm. Sci. Eng. Appl. **5**, 021004 (2013).
[31]V. Kumar, A. Srivastava, and S. Karagadde, "Compositional dependency of double-diffusive layers during binary alloy solidification: Full-field measurements and quantification," Phys. Fluids **30**, 113603 (2018).
[32]V. Kumar, G. S. Abhishek, A. Srivastava, and S. Karagadde, "On the mechanism responsible for unconventional thermal behaviour during freezing," J. Fluid Mech. **903**, A32 (2020).
[33]D. Anderson and M. G. Worster, "A new oscillatory instability in a mushy layer during the solidification of binary alloys," J. Fluid Mech. **307**, 245–267 (1996).
[34]P. Guba and M. G. Worster, "Interactions between steady and oscillatory convection in mushy layers," J. Fluid Mech. **645**, 411 (2010).
[35]K. Roy, R. Ponalagusamy, and P. Murthy, "The effects of double-diffusion and viscous dissipation on the oscillatory convection in a viscoelastic fluid saturated porous layer," Phys. Fluids **32**, 094108 (2020).
[36]P. Guba and D. M. Anderson, "Diffusive and phase change instabilities in a ternary mushy layer," J. Fluid Mech. **760**, 634–669 (2014).
[37]J. Narski and M. Picasso, "Adaptive finite elements with high aspect ratio for dendritic growth of a binary alloy including fluid flow induced by shrinkage," Comput. Methods Appl. Mech. Eng. **196**, 3562–3576 (2007).
[38]A. Bhattacharya and P. Dutta, "Effect of shrinkage induced flow on binary alloy dendrite growth: An equivalent undercooling model," Int. Commun. Heat Mass Transfer **57**, 216–220 (2014).
[39]A. Bhattacharya, "Binary alloy dendrite growth in presence of shrinkage induced convection," Mater. Res. Express **6**, 126544 (2019).
[40]U. K. Sajja and S. D. Felicelli, "Modeling freckle segregation with mesh adaptation," Metall. Mater. Trans. B **42**, 1118–1129 (2011).
[41]W. Bennon and F. Incropera, "A continuum model for momentum, heat and species transport in binary solid-liquid phase change systems-I. Model formulation," Int. J. Heat Mass Transfer **30**, 2161–2170 (1987).
[42]W. Bennon and F. Incropera, "A continuum model for momentum, heat and species transport in binary solid-liquid phase change systems-II. Application to solidification in a rectangular cavity," Int. J. Heat Mass Transfer **30**, 2171–2187 (1987).
[43]K. Chiang and H.-L. Tsai, "Shrinkage-induced fluid flow and domain change in two-dimensional alloy solidification," Int. J. Heat Mass Transfer **35**, 1763–1770 (1992).
[44]A. D. Monde, O. Chawla, V. Kumar, S. Karagadde, and P. R. Chakraborty, "Shrinkage induced flow during directional solidification of pure substance in a bottom cooled cavity: A study on flow reversal phenomena," Phys. Fluids **32**, 047104 (2020).
[45]P. R. Chakraborty, "Enthalpy porosity model for melting and solidification of pure-substances with large difference in phase specific heats," Int. Commun. Heat Mass Transfer **81**, 183–189 (2017).
[46]S. Patankar, *Numerical Heat Transfer and Fluid Flow* (Taylor & Francis, 2018).
[47]P. K. Stansby, "Solitary wave run up and overtopping by a semi-implicit finite-volume shallow-water Boussinesq model," J. Hydraulic Res. **41**, 639–647 (2003).
[48]V. R. Voller and C. Prakash, "A fixed grid numerical modelling methodology for convection-diffusion mushy region phase-change problems," Int. J. Heat Mass Transfer **30**, 1709–1719 (1987).
[49]P. Sung, D. R. Poirier, and S. Felicelli, "Sensitivity of mesh spacing on simulating macrosegregation during directional solidification of a superalloy," Int. J. Numer. Methods Fluids **35**, 357–370 (2001).
[50]J. Guo and C. Beckermann, "Three-dimensional simulation of freckle formation during binary alloy solidification: Effect of mesh spacing," Numer. Heat Transfer, Part A **44**, 559–576 (2003).
[51]S. Geng, P. Jiang, X. Shao, G. Mi, H. Wu, Y. Ai, C. Wang, C. Han, R. Chen, W. Liu *et al.*, "Effects of back-diffusion on solidification cracking susceptibility of al-mg alloys during welding: A phase-field study," Acta Mater. **160**, 85–96 (2018).
[52]Z.-H. Lee, B. Lee, M. Kang, S. Chung, and S. Coriell, "Experimental investigation of convection during vertical bridgman growth of dilute Al-Mg alloys," J. Crystal Growth **141**, 209–218 (1994).
[53]J. Liu, H. P. Duarte, and S. Kou, "Evidence of back diffusion reducing cracking during solidification," Acta Mater. **122**, 47–59 (2017).
[54]A. Mo and H. J. Thevik, "Simplified computation of macrosegregation in multicomponent aluminum alloys," Metall. Mater. Trans. A **29**, 2189–2194 (1998).
[55]R. Trivedi, S. Liu, P. Mazumder, and E. Simsek, "Microstructure development in the directionally solidified al–4.0 wt% Cu alloy system," Sci. Technol. Adv. Mater. **2**, 309–320 (2001).
[56]H. Kato and J. Cahoon, "Inverse segregation in directionally solidified Al-Cu-Ti alloys with equiaxed grains," Metall. Trans. A **16**, 579–587 (1985).
[57]J. Dagner, J. Friedrich, and G. Müller, "Numerical study on the prediction of microstructure parameters by multi-scale modeling of directional solidification of binary Aluminum–Silicon alloys," Comput. Mater. Sci. **43**, 872–885 (2008).
[58]B. Willers, S. Eckert, P. A. Nikrityuk, D. Räbiger, J. Dong, K. Eckert, and G. Gerbeth, "Efficient melt stirring using pulse sequences of a rotating magnetic field: Part II. Application to solidification of Al-Si alloys," Metall. Mater. Trans. B **39**, 304–316 (2008).
[59]J. Jain, A. Kumar, and P. Dutta, "Numerical studies on channel formation and growth during solidification: Effect of process parameters," J. Heat Transfer **129**(4), 548–558 (2007).

[60]T. Hattori, N. Bartos, S. Norris, M. Kirkpatrick, and S. Armfield, "Experimental and numerical investigation of unsteady behaviour in the near-field of pure thermal planar plumes," Exp. Thermal Fluid Sci. **46**, 139–150 (2013).
[61]J. M. Lopez and F. Marques, "Instability of plumes driven by localized heating," J. Fluid Mech. **736**, 616–640 (2013).
[62]H. Yang, "Buckling of a thermal plume," Int. J. Heat Mass Transfer **35**, 1527–1532 (1992).
[63]J. Heinrich, U. Sajja, S. Felicelli, and D. Westra, "Projection method for flows with large local density gradients: Application to dendritic solidification," Int. J. Numer. Methods Fluids **57**, 1211–1226 (2008).